

A Structural and Optical Look at Functional Materials



Mustafa Kemal Ozturk

Abstract This chapter is an introductory chapter which presents overviews of the main methods in analyzing, producing, and characterizing functional materials. A brief idea about deducing optical properties from dielectric function using Kramers–Kronig relations is presented, with $\text{Be}_x\text{Zn}_{1-x}\text{Te}$ alloys as an example. The reflectance, transmittance, real and imaginary parts of the dielectric function, refractive index, extinction coefficient, absorption coefficient, and loss function of these alloys are plotted against energy and discussed. Brief ideas about some growth techniques of single crystals such as Bridgman, Czochralski, and Kyropoulos are overviewed. Besides, some deposition methods of films are described. These include molecular beam epitaxy (MBE), metal–organic chemical vapor deposition (MOCVD), and chemical vapor deposition (CVD). Moreover, the main characterization techniques X-ray diffraction (XRD), X-Ray reflectivity (XRR), scanning electron microscopy (SEM), X-ray fluorescence (XRF), small and wide-angle X-ray scattering (SAXS and WAXS), secondary ion mass spectroscopy (SIMS), atomic force microscopy (AFM), spectroscopic ellipsometry (SE), photoluminescence spectroscopy, Fourier transform infrared spectroscopy (FTIR), Raman Spectroscopy, UV-Vis spectroscopy, and others are briefly described, and some examples are presented.

Keywords Functional materials · Growth techniques · Characterization techniques · Structural properties · Optical properties

1 Introduction

When we look at the interaction of light and matter in nature, color spectrum formed according to lattice length of material after the light is absorbed by it and is caused by the optical behavior of the material. When we hit also to different materials with our hand slightly, we notice that different sounds come out from the material. This is

M. K. Ozturk (✉)

Photonics Application and Research Center, Department of Physics, Faculty of Science, Gazi University, 06500 Ankara, Turkey

e-mail: ozturkm@gazi.edu.tr

© Springer Nature Switzerland AG 2021

S. J. Ikhmayies et al. (eds.), *Advances in Optoelectronic Materials*,

Advances in Material Research and Technology,

https://doi.org/10.1007/978-3-030-57737-7_1

related with the acoustic property of the material. Furthermore, materials have such properties as having friction very near to zero, high electron mobility, superconductivity at low temperatures, responding to sunlight, sensitivity to light and movement, piezoelectric behavior producing current dependent on movement, producing current by cooling or heating (Peltier) or just the opposite, cooling or heating by current, storing data by spin behaviors, remembering original shape (shape memory effect), mechanical resistivity, and elastic properties. For this reason, the functional properties of the material, today scientists and Investigation and Development workers pay great attention on investigation of material properties. For developing nano-scale optoelectronic devices, related incredible studies take place in literature. For these developments, spectroscopic techniques are used intensively and it gave way to new electronic devices in nano-scale. By the help of these, nanoscale solar cells, paints, drugs, self-cleaning clothes and walls, nanorobots, smart TV, smart phone, and smart glass, and many other industrial products are designed. Studies on these subjects are continuing. After the first lamp transistor used in primitive radio and calculator, developing of diodes and binary system (1 right, 0 false) radios and TVs got smaller and faster and took their place in people's lives with great velocity. Later 4, 8, 16, 32, 64, and 128-bit systems are introduced, and dimensions of the devices got smaller and smaller. Computers, radios, TVs, mobile phones, smart phones, and many other smart devices became a piece of our lives very fast. These developments are usually traced by patents, and till now, many patents are produced. For this reason, mentioning people here who have the most patents will be useful. Making a simple search on net by the year 2018, one can reach this knowledge on many Web sites. Kia, Siver, and Brook took 4732 patents on mostly, digital materials, electronic devices, LCD, security inks, chemistry, DNA, mechanics, and press between 1994 and 2017 years. Shunpei YAMAZAKI follows these with 4315 patents on solar panels, flash memories, and liquid screens. As the third, Paul LAPSTUN took 1278 patents on press, digital paper, electronic, and Internet fields.

During the growth of technology, elements which the material science is focused on are II–VI groups on periodic table and compound semiconductor materials formed by them. Of course polymers and organic materials also take attention. Semiconductors are structurally good crystals. Atoms and molecules form a base on a point of crystal, and this base is called the lattice. 3D settlement of these lattices forms the crystal. The most important property of this crystal is symmetry. And symmetric operations are given as reflection, rotation, and inversion in structure. There are seven different types of lattice; the general lattice kind of these is triclinic due to point symmetry. These lattice types are very important in terms of functional properties of solids. Stable cubic and hexagonal semiconductors are preferred due to their structural, electrical, and optical properties. These materials may present different electrical and optical properties according to their lattice structure. Here, mobility of free orbital electron movement determines the electrical properties. For the atoms which are suitable for disturbing, electronic transitions between energy levels are related with forbidden band gap and optical properties. Besides, smoothness of the surface and to see sun light in colored spectra indicates a successful growth period, else cracked and rough surface structure can be seen. Lattice mismatch and fault

structure of the crystal formed on these circumstances change the optical behavior of the structure. Lattice settlement of the crystal is caused by the vibrational phonon movements. Lattice vibrations are called phonons. Phonon movements belonging to structure, elastic constants of the crystal structure, phonon frequency, and stable stress show different properties, and these properties may change by faults. Semiconductors may be in crystal, polycrystalline, or amorphous structure. In further investigations, for growth procedure of the semiconductor, it is desired that it should have good optical and electrical behaviors. With different crystal growth techniques, it is possible to grow more stable epitaxial layers under high vacuum and at high temperatures. Semiconductors may be grown as cubic and hexagonal structures (Si, Ge, GaAs, GaN, ZnO, GaP, GaInP AlGaAs, AlN, GaN, InGaN, AlInN, AlGaIn, etc.) in MBE or MOCVD systems with high crystallized epitaxial layers. Light-emitting diode, high electron mobility transistor, photo detector, sensors, and diodes may be formed in heterostructure as quantum wells and multi-quantum wells. Cubic structure crystal semiconductor materials as Si, Ge, InP, GaP, GaAs, AlGaAs, and InGaAs are the first-generation investigation materials. These materials are still used for production of optoelectronic devices in nanotechnology field. But because they have very narrow structural and optical properties, this sector went on looking for new materials. In these investigations apart from the materials mentioned above which do not have cubic crystal structure, interest on GaN-based hexagonal systems which have resistivity against high temperature, frequency, and voltage is increasing. Of course, the first problem noticed is c-oriented lattice mismatch between epitaxial layer and Al_2O_3 substrate which disorders the stability of the material. While lattice mismatch causes lattice relaxation, dislocations increase to a very serious level, and finally, this failure causes cracks on the surface. Furthermore, while cooling from growth temperature to room temperature, bending movements with wide dislocations are seen together with mosaic defects (such as layer tilt angle, twist angle, and crystallized blocks). Because of this, full width at half maximum (FWHM) value for (002) symmetric plane for GaN layer used as buffer layer increases above 400 arcsec ($1^\circ = 3600$ arcsec). Of course, these problems may be overcome by growing cut-thickness GaN layers in order to decrease the lattice mismatch of AlN and GaN nucleation layers at low temperatures to prevent dislocations moving on c-direction. By the help of these improvements, GaN-based AlGaIn/GaN mixed structure field-effect transistors (HFET) , AlGaIn/GaN mixed junction bipolar transistors, GaN metal oxide semiconductor field-effect transistors, Schottky and p-i-n rectifiers are used as new generation optoelectronic devices [1–7] . Recently, S.V. Novikov and coworkers succeeded in the growth of GaN and AlGaIn epitaxial layers on GaAs with MBE without surface cracking [8] . Although III–V group compounds with nitrogen are a wide research area, ZnS, CdS, HgTe, CdTe, and CdHgTe alloys from II to VI group are a newer research area [9]. Besides, double and triple semiconductors formed by using La, Hf, Ru, Tm, Si, Ge, Li, Pt atoms are a research area for more daily optoelectronic devices [10].

2 Theoretical Optical Approach to Functional Materials

When the material is exposed to electromagnetic waves, as a result of interaction of electrons with wide spectrum, some optical events occur. If the energy which the spectrum has is equal to forbidden band gap E_g , the electron found in orbital is disturbed to a higher energy level. If the energy is lower than the forbidden energy band gap, instead of absorption, spectrum is transmitted, and this material is called transparent [11]. Transmission or absorption of a photon is related with electron configurations of semiconductor, metal, or insulator [12]. Dielectric property of the material is a measure of insulation, and forbidden band gap determines whether the material is an insulator or a conductor. For this reason, by calculating the dielectric constant of the material, one can gain knowledge about optical behaviors of this material. Absorption of incident spectrum by the material has some periods. The reason for the absorption is electron transmissions of optical energy in the material's fundamental forbidden band borders. Absorption of the spectrum is excitation of surface electrons, transmitted between bands with optical energy, in a bulk material. Transition between bands can be seen in every material. That is, optical properties of a material are related with electron density in transition situations and band structures of that material [13]. There are many models for numerical optical behaviors of the material. All these models have better properties and calculation conveniences. One or more of these models can be calculated in detail with many programs—for example, Drude model, Lorentz model, Induced field-effect method, Debye relaxation, Kramer–Kronig equations, Hagen–Rubens equation. Calculations can be done by using the mentioned approximations above [14]. These models given for optical properties are the most frequent used ones. Here, the Kramer–Kronig equations are given, and then, an example of using it is presented.

2.1 Kramers–Kronig Relations

Kramers–Kronig relations are used to calculate the real part from the imaginary of a complex function or vice versa. So, the dielectric function ($\varepsilon = \varepsilon_1 + i\varepsilon_2$) which is a function of frequency ω , has a real part $\varepsilon_1(\omega)$ and imaginary part $\varepsilon_2(\omega)$. Any of them can be used to produce the other [14]. For example

$$\varepsilon_1(\omega) = 1 + \frac{2}{\pi} \int_0^{\infty} d\omega' \frac{\omega'^2 \varepsilon_2(\omega')}{\omega'^2 - \omega^2} \quad (1)$$

Kramers–Kronig relations are also to relate the real and imaginary portions for the complex refractive index $n^*(\omega) = n(\omega) + i\kappa(\omega)$. Also, they allow to calculate the reflectivity, energy loss function $L(\omega)$, and absorption coefficient $\alpha(\omega)$ all as functions of frequency or energy.

Refraction index $n(\omega)$ and extinction coefficient $\kappa(\omega)$ can be determined using the components of dielectric function;

$$n(\omega) = \left[\sqrt{\varepsilon_1^2(\omega) + \varepsilon_2^2(\omega)} + \varepsilon_1(\omega) \right]^{1/2} / \sqrt{2} \quad (2)$$

$$\kappa(\omega) = c \left[\sqrt{\varepsilon_1^2(\omega) + \varepsilon_2^2(\omega)} - \varepsilon_1(\omega) \right]^{1/2} / \sqrt{2} \quad (3)$$

Reflectivity $R(\omega)$ and absorption coefficient $\alpha(\omega)$ can be calculated using the following equations:

$$R(\omega) = \left[\frac{\sqrt{\varepsilon_1^2(\omega) + j\varepsilon_2^2(\omega)} - 1}{\sqrt{\varepsilon_1^2(\omega) + j\varepsilon_2^2(\omega)} + 1} \right]^2, \quad (4)$$

$$\alpha(\omega) = \sqrt{2\omega} \left[\sqrt{\varepsilon_1^2(\omega) + \varepsilon_2^2(\omega)} - \varepsilon_1(\omega) \right]^{1/2} \quad (5)$$

and energy loss function $L(\omega)$ is identified by the following formula:

$$L(\omega) = \text{Im} \left[\frac{-1}{\varepsilon(\omega)} \right] = \varepsilon_2(\omega) / [\varepsilon_1^2(\omega) + \varepsilon_2^2(\omega)] \quad (6)$$

2.1.1 Optical Properties of $\text{Be}_x\text{Zn}_{1-x}\text{Te}$ Alloys

$\text{Be}_x\text{Zn}_{1-x}\text{Te}$ is formed by II–VI group atoms and used for blue-green laser diode production. This structure can be grown in MBE growth system with Be, Zn, and Te sources. In this part, optical properties, static dielectric constants, refraction indexes, absorption coefficients, and plasmon frequency values are calculated according to x alloy ratio as examples [15].

Dielectric Functions

The value for starting absorption of imaginary part of dielectric function for $\text{Be}_x\text{Zn}_{1-x}\text{Te}$ gives the splitting $\Gamma_v - \Gamma_c$. Also, it represents the direct optical transition between valance band and conduction band. On the other hand, these values are the same with band gap [16]. Real and imaginary parts of the dielectric function for $\text{Be}_x\text{Zn}_{1-x}\text{Te}$ are given in Fig. 1. As shown in this figure for $\text{Be}_{1-x}\text{Zn}_x\text{Te}$, the main peaks for real part of the dielectric function are 3.54, 2.79, and 2.37 eV for $x = 0.25$, 0.50, and 0.75 doping values, respectively. For $\varepsilon_1(\hbar\omega) = 0$, energy values 7.29, 8.43,

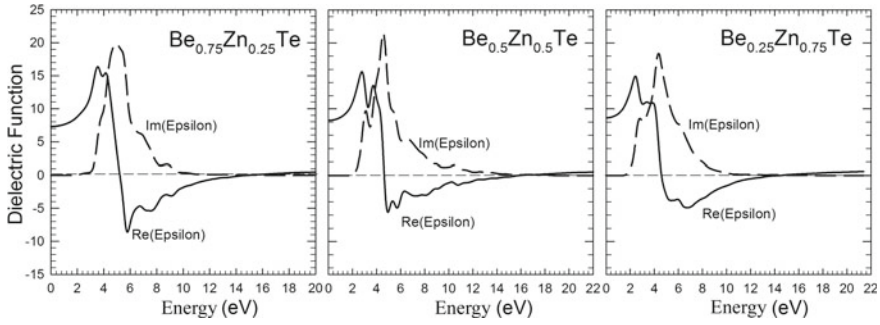


Fig. 1 Real and imaginary parts of dielectric constant for $\text{Be}_{0.75}\text{Zn}_{0.25}\text{Te}$, $\text{Be}_{0.5}\text{Zn}_{0.5}\text{Te}$ and $\text{Be}_{0.25}\text{Zn}_{0.75}\text{Te}$ alloys against energy

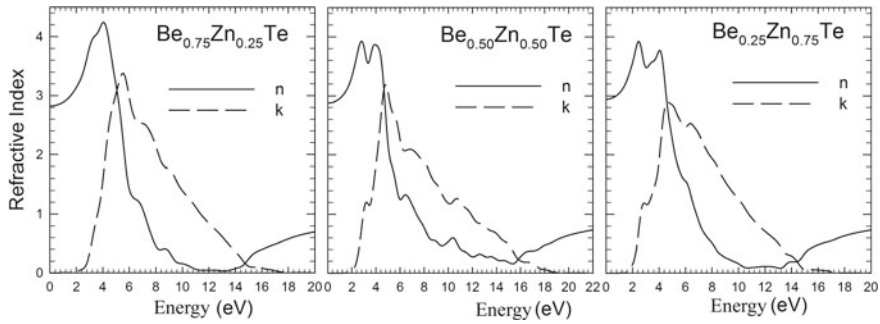


Fig. 2 Refractive index (n) and extinction coefficient (k) for $\text{Be}_{0.75}\text{Zn}_{0.25}\text{Te}$, $\text{Be}_{0.5}\text{Zn}_{0.5}\text{Te}$, and $\text{Be}_{0.25}\text{Zn}_{0.75}\text{Te}$ alloys against energy

and 8.75 eV give static dielectric constant for increasing Be doping values $x = 0.25$, 0.50, and 0.75, respectively. The imaginary part of the dielectric constant begins to increase at about 2.04, 2.11, and 1.58 eV according to doping values. These values are near to band gap energy. This situation represents the optical transition between valance band and conduction band. The alloy acts as a transparent material until the value where dispersion curve started to increase. Here is the low dispersion region. The energy values for the maximum of the imaginary part of the dielectric constant are at 4.96, 4.5, and 4.37 eV for the doping values 0.25, 0.50, and 0.75, respectively. These values correspond to interband transitions [17, 18].

Refractive Index and Extinction Coefficients

Variation of refractive index $n(\hbar\omega)$ and extinction coefficient $k(\hbar\omega)$ for $\text{Be}_x\text{Zn}_{1-x}\text{Te}$ are given in Fig. 2 The region where refractive index $n(\hbar\omega)$ is maximum shows the transparent region. The value of refractive index at zero frequency is $n(0)$, and the square of $n(0)$ equals to the isostatic real dielectric coefficient $\epsilon_1(0)$. It is seen that ϵ_1

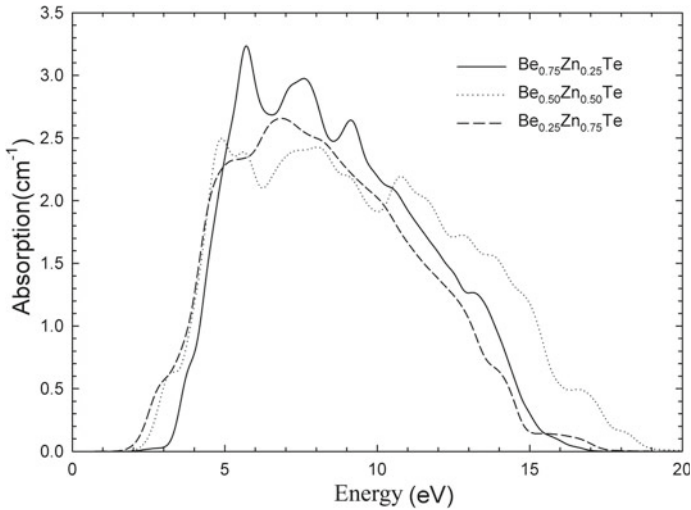


Fig. 3 Absorption coefficient for $\text{Be}_{0.75}\text{Zn}_{0.25}\text{Te}$, $\text{Be}_{0.5}\text{Zn}_{0.5}\text{Te}$, and $\text{Be}_{0.25}\text{Zn}_{0.75}\text{Te}$ alloys against energy

(0) and $\{n(0)\}^2$ are in accordance with each other for $\text{Be}_x\text{Zn}_{1-x}\text{Te}$. Also, it is seen that maximum value of extinction coefficient of alloys $k(\omega)$ and static dielectric constant which $\epsilon_1(0)$ corresponds to zero energy are in accordance with each other. Dispersion curves of refraction index for $\text{Be}_{1-x}\text{Zn}_x\text{Te}$ are shown in Fig. 2, and values of $n(0)$ are found as 2.85, 2.89, and 2.95 for $x = 0.25, 0.50,$ and 0.75 , respectively. It is understood that when the value of Zn increases, refractive index also increases. It is seen that real part of dielectric function and refractive index and imaginary part of the dielectric function and extinction coefficient are in agreement with each other.

Absorption Coefficient

Absorption coefficient defines absorption of light by the materials per unit length. The limit of the absorption is related to optical transitions between fundamental band gaps. Interband absorption is the excitation of a solid material electron, transmitting optically between bands. Absorption coefficient is obtained from the real and imaginary parts of the dielectric function as shown in Eq. (4), and the results are shown in Fig. 3 for $\text{Be}_{1-x}\text{Zn}_x\text{Te}$ alloys. Absorption coefficient values are starts to increase at 2.06, 2.11, and 1.56 eV for $\text{Be}_{1-x}\text{Zn}_x\text{Te}$, respectively, according to x doping values. It is seen that the point where the absorption coefficient started to increase agrees with those when the imaginary part of the dielectric function and the extinction coefficient began to increase.

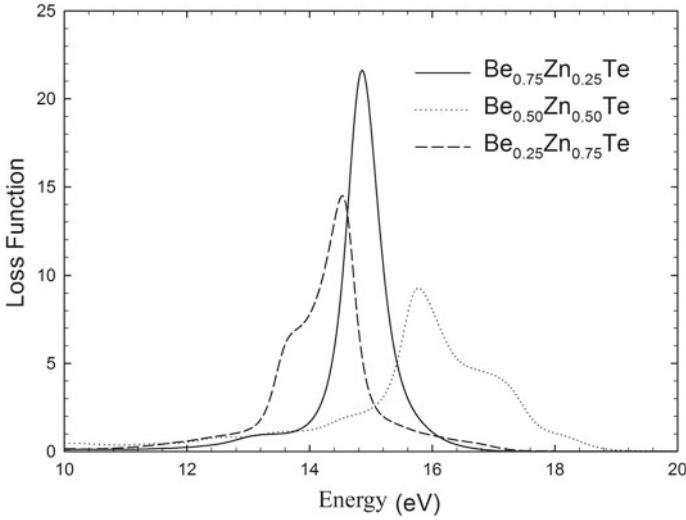


Fig. 4 Loss function $L(w)$ for $\text{Be}_{0.75}\text{Zn}_{0.25}\text{Te}$, $\text{Be}_{0.5}\text{Zn}_{0.5}\text{Te}$, and $\text{Be}_{0.25}\text{Zn}_{0.75}\text{Te}$ alloys against energy

Loss Function Calculation

Loss function variation with energy is given in Fig. 4 for $\text{Be}_x\text{Zn}_{1-x}\text{Te}$. It is the variation of loss energy while the electron is transmitting from the top of the valence band to the bottom of the conduction band. Here, the main peak value is known as *plasmon frequency*. Alloys act as insulators above plasmon frequency value and as metals below plasmon frequency value.

Loss function of the electron is deduced from the real and imaginary parts of the dielectric function for $\text{Be}_{1-x}\text{Zn}_x\text{Te}$ alloys, and it is shown in Fig. 4. Loss function has some peaks between 12 and 19 eV. The frequency corresponding to the main peak of the loss function is called as plasmon frequency. Imaginary part of the dielectric function is minimum where the peak of loss function is maximum. For the doping values ($x = 0.25, 0.5, \text{ and } 0.75$), the energies corresponding to plasmon frequency values are 14.80, 15.70, and 14.48 eV. When we look at the plots, it is seen that absorption is too little between 0 and 12 eV. The reason is that there is absorption in this frequency range as can be deduced from the imaginary part of the dielectric function [19].

3 Growth Techniques of Functional Materials

Semiconductor technology has become quite common today. For this reason, the optoelectronic devices desired to be obtained are very much concerned with the

formation of single crystalline structures such as group III–V, II–VI for the epitaxial layers. Formation of single crystalline materials has become possible by various crystalline growth methods. Thin films can be grown with sophisticated and simple techniques. Crystalline growth methods are divided into bulk and thin film growth. Bulk growth techniques are Bridgman and Czochralski. Thin film growth techniques are generally molecular beam epitaxy, metal–organic chemical vapor deposition, and chemical vapor deposition techniques.

3.1 Bulk Crystalline Growth Techniques

Techniques for single crystalline growth are solution growth, melt growth, and vapor growth techniques [20]. In cubic or hexagonal systems, crystals oriented in a desired orientation and additive density is grown on a core crystal (AlN, ZnSe, CdSe, GaAs, GaP, Ge, S, GaN, Al₂O₃, etc.). Brief ideas about some of these techniques will be given below.

3.1.1 Bridgman Technique

In Bridgman technique, the crystal is grown in a vacuum quartz tube surrounded by a crystal oven or thermos elements. By the Bridgman method, the crystalline surface, which is solidified by crystallization, is moved in the vertical direction, and the pointed end in the furnace or quartz tube is lowered. The pointed tip is the starting point for the first cooling and acts as a core during the growth. By pulling the pointed end, the crystal in molten state is enlarged [20]. In the Bridgman technique, the oven or quartz tube can be moved by holding the crystal carrier stationary. The crystal carrier can be moved by holding the furnace or quartz tube constant, or it is possible to grow the crystal by different methods by simply changing the temperature without movement.

3.1.2 Czochralski (CZ) Technique

Czochralski is a fast method to grow single crystals. It is widely used for semiconductors, oxides, and fluorides to be used in optical applications. This method is the most widely used technique in the production of single crystalline silicon (Si), and germanium (Ge) is the Czochralski (CZ) technique [21]. Ultra-high-purity Si is usually dissolved in a carrier which is quartz. If n-type or p-type single crystalline Si is grown, then additive atoms such as boron (B) or phosphorus (P) are added in this step. A Si single crystal (which can be expressed as a seed crystal) in a suitable crystal orientation is immersed in the melt and is slowly rotated and pulled up at the same time. With the CZ method, it is possible to obtain a single crystal in a very large cylindrical shape. This method is often used in the growth of silicon single crystals.

This method produces the most homogeneous and perfect crystals. But it is only applicable to the materials that melt congruently or nearly congruently, because the solid and melt compositions are the same at equilibrium.

3.1.3 Kyropoulos Technique

The Kyropoulos technique was designed to create a smooth crystal at low temperatures in the mid-twentieth century. This technique is one of the most advanced techniques for growing large single crystals before CZ technique. The most important difference between this technique and the CZ technique is that it can form different crystal forms. In Kyropoulos method, a solution in the pot is heated. By slowly cooling the melt, the solid–liquid interface between the melt and the core crystal begins to form. At the beginning of the crystal formation process, the nucleus forms a cone-shaped shape in the crystal aligned to the melt. In this method, instead of pulling up the crystal from the melt, the growth in the crucible is completed by cooling slowly. The size of the resulting crystal is almost equal to the diameter of the pot [22].

3.2 Thin Film Growth Techniques

3.2.1 Molecular Beam Epitaxy (MBE)

MBE is an ultra-high vacuum (UHV) -based thin film growth technique used to produce single-step, controlled, and high-quality epitaxial structures. It has become a widely used technique for the production of semiconductors, superconductors, and metals with a high degree of purity. The underlying phenomenon of the MBE growth system is quite simple: The solid source materials are placed in the evaporation channels to provide angular distributions of atoms or molecules. The substrate is heated to the desired temperature, and the substrate is rotated for growth to be homogeneous. The ultra-high vacuum hits the substrate surface heated in the environment and is bonded to the structure on the enlarged surface. Despite its conceptual simplicity, material purity and slow growth are a bad advantage, but it is a significant advantage that growth can be controlled through the system. In the MBE system, such as GaAs, AlGaAs, InGaAs, InGaP, InP, AlGaN, and AlGaAsP structures can be grown [23].

3.2.2 Metal–Organic Chemical Vapor Deposition (MOCVD)

MOCVD is chemical vapor deposition method for epitaxial growth of materials, exclusively compounds. The growth of crystal structures in the MOCVD technique occurs chemically. As an example, the GaAs film growth is as follows: gallium (Ga) or arsenic (As) compounds, called precursor gases. Usually, a metal–organic

compound such as arsenic hydride (AsH_3) for As and trimethyl gallium (TMGa) for Ga is used. The precursor gases are injected into the reactor via the carrier gas (hydrogen or nitrogen). The reactor and substrate are heated to a certain temperature. Temperatures may range from about 500–1500 °C depending on the material to be produced. Reaction in the heated reactor and sub-surface occurs in the gas phase. The particles, together with AsH_3 and TMGa, are transported to the substrate surface where they are deposited on the substrate and the remaining gases are discarded. Within these steps, the GaAs layer grows on the buffer layer. Unreacted molecules are separated from the surface and discharged from the reactor with the aid of carrier gas [24, 25].

As a sample, the high-resistivity GaN layers were grown on 6H-SiC substrates, with different buffer layers structures in MOCVD system. For these structures, trimethylaluminum (TMAI), TMGa, and ammonia (NH_3) as Al, Ga, and N precursors are used, respectively. Oxide layer in surface of SiC substrate was removed by annealing of the under hydrogen ambient at 1200 °C for ~10 min. For four different samples (called A, B, C and D), growth procedure is applied with different buffer layers. All of the samples nominally contain a 190 Å thick GaN layer after the buffer structures (Table 1).

Sample A contains 100 Å-thick, low temperature growth AlN, 1400 Å-high temperature growth AlN and 500x100 Å GaN/AlN pair super lattice structures under high-resistant GaN layer. In sample B, 100 Å-low temperature AlN and 1400 Å AlN layers were grown as a buffer layer at high temperature. The buffer layers of sample C includes a 100 Å-thick AlN nucleation layer grown at low temperature (705 °C) and 2300 Å-thick AlGaN layer. There, XRD scan was used to obtain the Al content of the $\text{Al}_x\text{Ga}_{1-x}\text{N}$ layer, and its value is determined as 67.0%. And 300 Å-thick AlN (high-temperature AlN) is grown at 1100 °C and is used as a buffer layer in sample [26].

Table 1 High-resistant GaN barrier structures designed in the different structural properties

A	B	C	D
High-resistivity GaN layer 190 Å	High-resistivity GaN layer 190 Å	High-resistivity GaN layer 190 Å	High-resistivity GaN layer 190 Å
GaN/AlN superlattice 500 Å	–	Undoped-AlGaN layer 2300 Å	–
High-temperature AlN layer 1400 Å	High-temperature AlN layer 1400 Å	–	High-temperature AlN layer 3000 Å
Low-temperature AlN nucleation 100 Å	Low-temperature AlN nucleation 100 Å	Low-temperature AlN nucleation 100 Å	–
Semi-insulation 6H-SiC substrate	Semi-insulation 6H-SiC substrate	Semi-insulation 6H-SiC substrate	Semi-insulation 6H-SiC substrate

3.3 Chemical Vapor Deposition (CVD)

CVD is a process in which gases chemically react and form reaction products on the substrate surface. The basic process steps in CVD are [27]: (I) Transport of reaction materials to the reaction chamber. (II) Chemical reaction at the sample surface. (III) Accumulation of reaction products on the heated surface of the sample. (IV) Separation of residual gases from the sample surface.

3.4 Vapor Phase Epitaxy (VPE)

VPE is a chemical vapor deposition method on a substrate for epitaxial solid layers. There are two methods of growing groups III and V with VPE: chloride and hydride. In the chloride method, chlorine is passed through the gallium arsenic metal to form GaCl_3 . In the hydride method, hydrogen is mixed with arsenic (AsH_3) and GaCl_3 gases and sent on the substrate, which is held on a rotating plate at about 1100 K. The gases are trapped on the substrate surface. The enlargement of structures such as GaAs by the VPE method can create a perfect crystal with a better purity [28].

3.5 Liquid Phase Epitaxy (LPE)

LPE is based on the decomposition of sub-solid material from a cooling solution layer. The substrate is stored in the growth chamber, and the solution is saturated with the growth medium until the desired growth temperature is reached. The solution is then contacted with the single crystalline substrate surface, allowed to time for the desired growth to occur, and finally, the material is allowed to cool after growth has occurred [29].

4 Characterization Methods of Functional Materials

4.1 Scanning Electron Microscopy (SEM)

In this system, electrons are thermionically emitted from an electron gun fitted with a tungsten filament. The emitted electrons which have an energy of 5–30 keV are accelerated with the help of electrical force, which is reversely directed to the electric field, and these electrons are bombed by means of focusing lenses toward the surface of the material, which is coated with one of Au, Pt, Ag, and Cu metals (Fig. 5). Because of this situation, two types of collisions are seen that are elastic and inelastic.

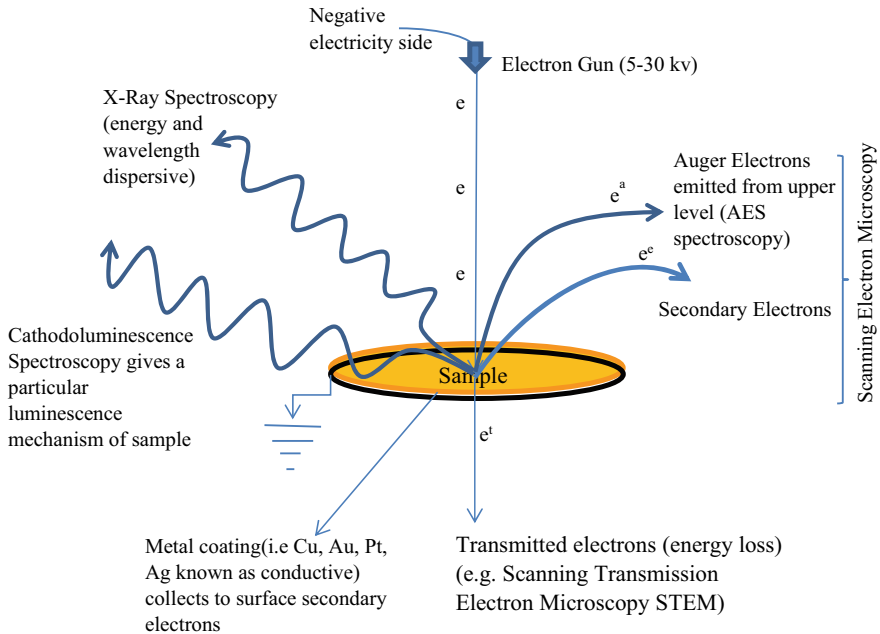


Fig. 5 SEM diagram and spectroscopy techniques by electron-material interactions

SEM and spectroscopic techniques are related to inelastic collisions. In inelastic collisions, electron interacts with the atoms of the sample material. Incident electron rips an electron which may be of 1 s core energy level and passes to the back side of the sample by losing most of its energy. These electrons give the opportunity of scanning transmitted electron microscopy (STEM) image. The electron ripped from 1 s is known as the secondary electron. Secondary electrons may also result from other inelastic interactions between the primary electron beam and the sample. Secondary electrons which are ripped from the atoms approximately 10 nm down the surface of the material are taken to the surface by the help of coated metals, and they radiate on the surface of the material with the kinetic energy they have. Conductor metal collects the electrons on the surface, and so, there are no charges inside. Electrons on the surface make a wide radiation spectrum according to their energy density. Later, these radiations are transformed to image analyzers, amplifiers, and detectors [30].

As an example of scanning electron microscope images, Fig. 6 shows the SEM micrograph representative of the boron-doped polyvinyl alcohol-HfO₂ fibers in different voltages (14.0 and 28.0 kV). It can be observed that the formation of single fiber and cluster structure was the predominant morphology; only a large number of them show irregular fiber orientation, and the average fiber diameter was 670 nm [31].

In order to be stable, 1 s level takes an electron from 2 s or 2p levels. Energy difference between 2 s and 2p and 1 s levels rips an electron from upper levels of

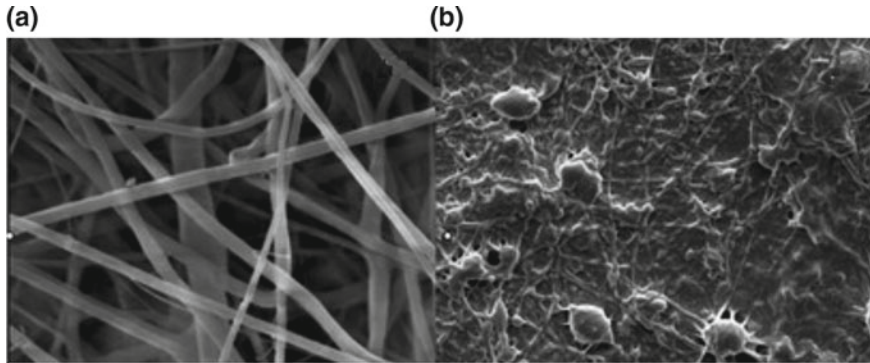


Fig. 6 SEM micrograph of polyvinyl alcohol-HfO₂ doped with boron which is synthesized by electrospinning technique at different voltages. **a** 14.0 kV, **b** 28.0 kV [31]

the atom, and this electron is called as Auger electron (Fig. 5). Auger comes from 1 to 3 nm thickness of the sample surface. Also, this situation causes emission of X-ray spectrum. Auger electrons are not seen in atoms such as lithium, helium, and hydrogen which do not have any electrons upper than p level. Auger electrons give the opportunity for both mineral analysis and surface analysis as (topography, morphology, composition, shape, etc.). This technique is called as Auger electron spectroscopy. X-ray spectroscopy caused from electronic transitions presents very useful analysis of elements. X-ray spectroscopy with energy and wavelength is known as EDX and WDS [32], respectively. Electron transition energies between stable levels are impaired with a database determined before, and one can decide which element these transitions belong to. Mapping can be done. Furthermore, ratio as a percentage of the compound in the composition can be determined. When the transition energies of the unknown samples are needed to be determined, one can use high-resolution fast semiconductor detector.

Figure 7 presents an example on EDX spectra, where the EDX spectra of CaO and SiO₂ are shown. If the CaO sample was examined by WDS, peaks would be sharper, and so, FWHM values would be lower.

Also, with EDX, one can do quantitative analysis, where EDX report gives the composition of the sample. For the example above, the composition of the sample is given in Table 2, where the concentrations of Si, Ca, and O elements are given by weight, atomic percent, and compound percent, respectively.

Cathodoluminescence in Fig. 5 is the term that describes the analysis of radiation emitted due to bombing the sample with electrons. By the help of cathodoluminescence spectroscopy, surface mapping can be done using deep energy values, and surface image can be formed. As an example, Fig. 8 shows the cathodoluminescence spectra of the p-GaAs reference substrate and the porous p-GaAs measured at room temperature. Porous GaAs layers are formed by electrochemical etching on highly doped p-type wafers with (001) crystal orientation by Bioud, et al. [33].

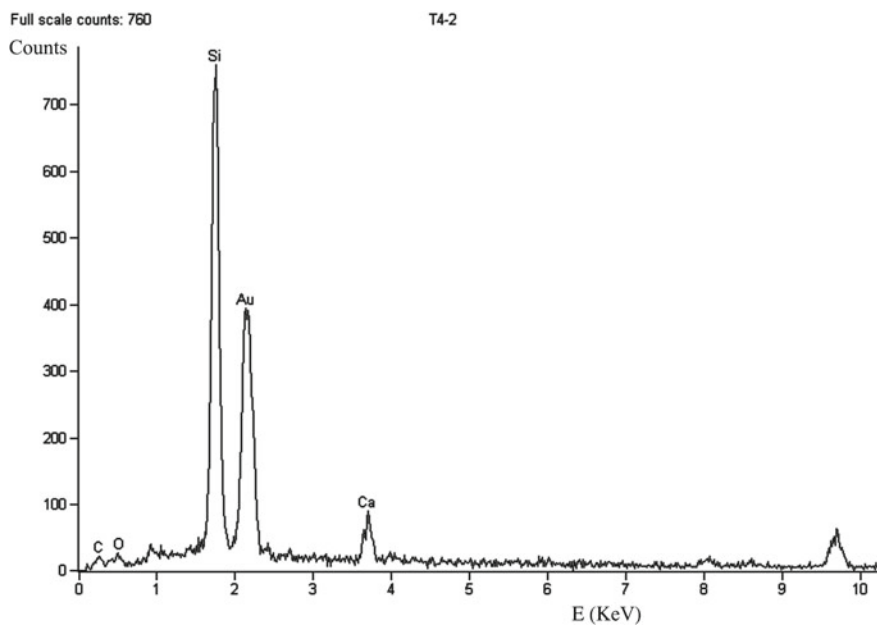
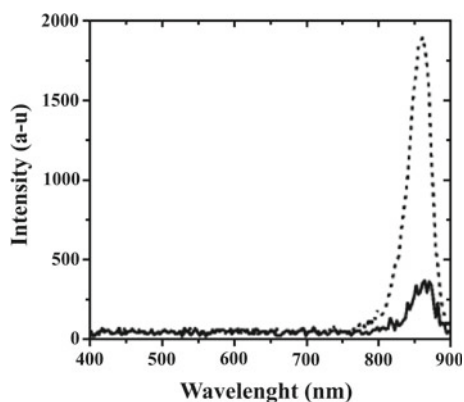


Fig. 7 EDX spectra of CaO and SiO₂

Table 2 EDX analysis for CaO and SiO₂

Element	Weight Conc %	Atom Conc %	Compound Conc %	Formula
O	51.06	65.58	0.00	O ₂
Si	42.59	31.16	91.12	SiO ₂
Ca	6.35	3.25	8.88	CaO

Fig. 8 Cathodoluminescence spectra at room temperature for the p-GaAs reference substrate and the porous p-GaAs [33]

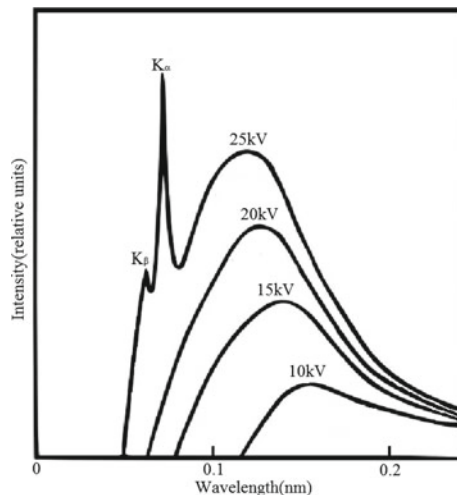


4.2 X-Diffraction and Spectroscopy

4.2.1 X-Ray Types

X-rays can be generated by an evacuated X-ray tube that uses a high voltage (~40 kV) to accelerate the electrons released by a hot cathode to a high velocity. The high-velocity electrons collide with the anode which is a metal target, such as Mo, Cu, Co, Fe, or Cr. X-rays are generated via interactions of the accelerated electrons with electrons of the anode. There are two types of generated X-ray: characteristic X-rays and bremsstrahlung one. The characteristic X-ray is produced when a high-energy electron collides with an inner shell electron (1S, 2S, ...), and both are ejected from the atom leaving a "hole" in the inner shell. This is filled by an outer shell electron with a loss of energy emitted as a monochromatic X-ray photon. If the inner shell is 1S (called K shell), and the outer shell is 2S, 2p (called L shells), then the emitted X-ray is called $K_{\alpha 1}$, but if the outer shell is 3s, 3p, 3d (called M shells), then the emitted X-ray is called $K_{\alpha 2}$. But if the inner shell is L shell, and the outer is M shell, then the X-ray is called $K_{\beta 1}$. If the outer shell in this case is 3s, 3p, 3d (called N shells), then the emitted X-ray line is called $K_{\beta 2}$, and so on. In other words, K_{α} is between L-K, K_{β} is between M-K, and K_{γ} is between N-K. In X-ray diffraction techniques, the sharpest peak, K_{α} , is used. K_{β} peak is absorbed by some filters such as Zr, Ni, Fe, Mn, and V. The second type of generated X-ray is produced when electrons pass near the nuclei in the anode material, where they slow down and loss their kinetic energy continuously. During their deceleration they give the continuous X-ray radiation known as a bremsstrahlung X-ray. As a result of characteristic and bremsstrahlung radiation, the generated X-ray will be similar to the one shown in Fig. 9. Characteristic X-ray peaks are the sharp peaks labeled as K_{α} and K_{β} . This

Fig. 9 Molybdenum X-ray spectrum with different potentials between the anode and cathode [34]



spectrum can be manipulated by changing the X-ray tube, current, or voltage settings, or by adding a filter to get monochromatic X-ray.

4.2.2 X-Ray Diffraction (XRD)

The X-ray diffractometer consists of three basic parts: an X-ray tube, a sample holder, and an X-ray detector, and it usually operates at known voltages and current. When a monochromatic beam of X-rays such as (K_{α}) is incident on a sample as shown in Fig. 10, it will be scattered from the atoms within the sample. To get monochromatic X-ray, a filter is required. K_{α} consists of $K_{\alpha 1}$ and $K_{\alpha 2}$, where $K_{\alpha 1}$ has a slightly shorter wavelength and twice the intensity as $K_{\alpha 2}$, so a weighted average of the two is used. If the material is crystalline, then the scattered X-rays will undergo constructive and destructive interference. This process is called diffraction, and the maxima of the intensity of diffracted X-rays, which correspond to constructive interference, are called diffraction peaks, and they satisfy Bragg's law:

$$2d \sin \theta = n\lambda \quad (7)$$

where d is the lattice spacing, θ is the diffraction angle, which is the angle between the incident X-ray and the scattering plane as shown in Fig. 10a. n is the order, and λ is the wavelength of incident X-rays. These diffracted X-rays are then detected by the detector, processed, and counted. The produced XRD pattern (diffractogram) is a fingerprint of the material under investigation. When a powder or polycrystalline

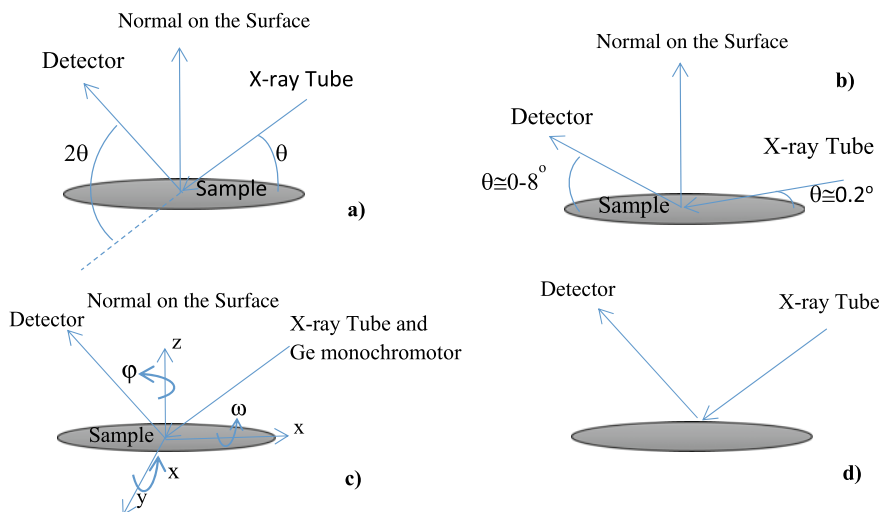


Fig. 10 **a** XRD measurement device scheme. **b** XRR measurement device scheme. **c** HRXRD, texture, and stress measurement device scheme. **d** XRF measurement device scheme

material with randomly oriented crystallites is placed in the X-ray beam, the beam will see all possible interatomic planes. By scanning the sample through a range of 2θ angles, all possible diffraction directions from the sample will be detected. The positions of the diffraction peaks can be converted to d-spacings, which allow the identification of the material by comparison with standard reference patterns [35].

X-ray diffraction is now a common technique for the study of crystal structures and atomic spacing. This technique provides information about structures, phases, preferred crystal orientations (texture), average grain size, crystallinity, strain, and crystal defects, and it is used for analyzing minerals, alloys, spreading phases, corrosion products, polymers, zeolites, explosives, and cement like materials. The parafocusing (or Bragg–Brentano) diffractometer is the most common geometry for diffraction instruments.

4.2.3 X-Ray Reflectivity (XRR)

The basic principle of X-ray reflectivity (XRR) is to reflect a beam of X-rays at grazing angles of incidence or low angles (typically, from 0 to 4° from grazing incidence) as shown in from a flat surface (Fig. 10b) and then to measure the intensity of reflected X-rays in the specular direction (reflected angle equal to incident angle) as a function of angle. The total external reflection occurs below the critical angle θ_c , which is very small, and depends upon the electronic density of the material. The higher the angle of incidence of the X-ray relative to θ_c , the deeper the X-rays penetrate into the material. Below the critical angle of total external reflection, X-rays penetrate only a few nanometers into the sample. At every interface where the electron density changes, a part of the X-ray beam is reflected. The interference of these partially reflected X-ray beams results in the oscillatory pattern observed in reflectivity experiments. From these reflectivity curves, layer parameters such as thickness (until 1000 nm), density (with %1 error), interface, and surface roughness (until 5 nm) for single and multilayer stacks on semiconductor wafers can be determined, regardless of the crystallinity of each layer (single crystal, polycrystalline, or amorphous). Also, morphology can be determined by spreading beam, correlation lengths, and fractal parameters.

Figure 11 shows a fit curve modified with dynamical equations of XRR scan for AlN crystal grown on SiC substrate by MOCVD method. The figure shows reflected intensity of X-rays against $2\theta/\theta$, where θ is the incidence angle and 2θ is the angle between the detector and incident X-rays. Here, by using fringes width thickness is found as 61.340 nm and by using amplitude of fringes roughness is found as 1.121 nm and density is found as 3.17 g/cm^3 .

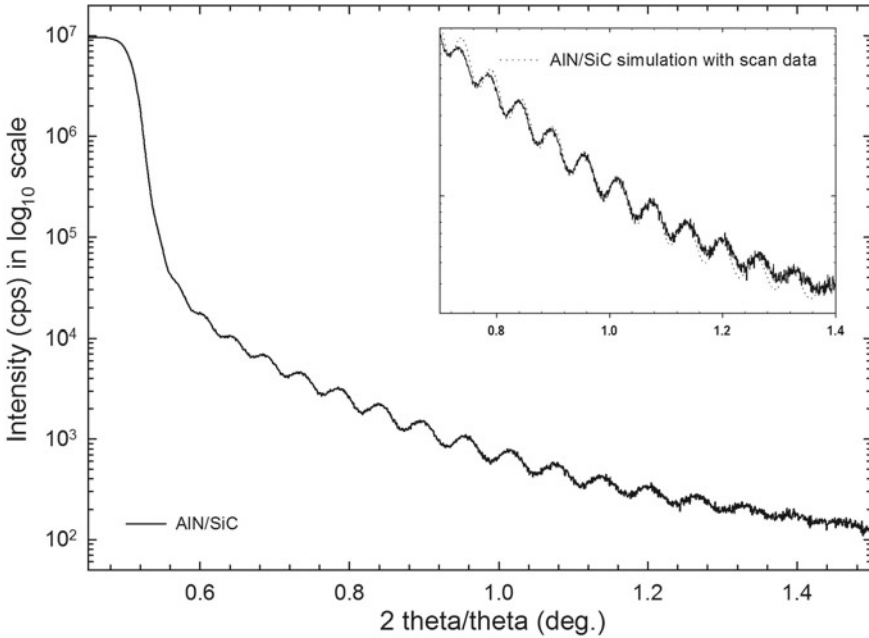


Fig. 11 Reflectivity scanning of AlN buffer layer grown on SiC by MOCVD. It is given with Inset fit value

4.2.4 High-Resolution X-Ray Diffraction (HRXRD)

HRXRD is an indispensable technique for semiconductor and polymer-semiconductor materials. HRXRD can be obtained using a laboratory-based triple-axis (four-circle) diffractometer. It requires a sealed X-ray tube or rotating anode, a mirror with a four-bounce duMond–Hart–Bartels (dHB) design monochromator to isolate $K_{\alpha 1}$ in the incident beam path, because in this method only $K_{\alpha 1}$ spectral line is used as X-ray source, and a two- or three-bounce monochromator in front of the detector. Usually, a Ge(220) crystal monochromator is used. A Ge(440) crystal monochromator can be used to further improve the resolution at the expense of intensity. Before describing the work principle of this method, it is essential to emphasize that the sample should be prepared very carefully. For an efficient $K_{\alpha 1}$, Ge monochromator, slit and absorber apparatus should be used. While inserting the sample and adjusting the detector, detector and $K_{\alpha 1}$ source tube should stand at the same axis level. Sample is attached to the Cradle attachment centered by the help of such methods as vacuum, clamp, glass paste, gum, or magnet. $K_{\alpha 1}$ beam in the detector is seen in full intensity value. During the z or height adjustment of the sample at the first time, when z approaches to beam, the total intensity value of the beam goes to zero. Here, the zero value of the total intensity, tube, and the X-ray beam direction behind the sample meet in attachment surface. Here, we shall adjust the direction of the X-ray beam toward the middle of the side section thickness of the sample. For

this reason, the middle of the getting zero full intensity value is calibrated as z value. Secondly, θ is scanned between -2 and $+2$, and the vision should be a triangle. Here, the aim is searching whether the surface of the sample has tilt or not. Sample adjustment is over if maximum peak point of the scan is at zero and it corresponds to the half of the full intensity value; otherwise, Z and θ scanning should be made again. Z axis-directed preferred planes are primarily examined by $\omega - 2\theta$ scanning for substrate, epilayer, heterostructure, MQW, and such nanotechnological devices. Data is taken from all layers and differentiated from each other. Among these planes, mostly c -directed symmetric (002), (004) and (006) planes are scanned. For example, while examining GaN layer, symmetric scans for these planes can be made.

In order to see crystal planes, sample will not be changed to powder, but it should be put into the system completely. For this reason, besides θ and 2θ , there should also be x , y , z , ω , χ , and φ axes (Fig. 10c), where ω is the angle between incident X-ray beam and the sample. HRXRD usually measures intensity of scattered X-rays as a function of ω and/or 2θ . There are different types of scans: first, a rocking curve which is a plot of X-ray intensity versus ω with the sample tilted, but the detector is set in an angle, second, a detector scan in which X-ray intensity is plotted against 2θ without changing ω (fixed source), and third, a coupled scan in which scattered X-ray intensity is plotted against 2θ , but if sample rotates, the detector also rotates, or in other words, ω changes in a way that is linked to 2θ . In this scan, the source is fixed, and $2\theta = 2\omega + \text{offset}$. It shall be noticed that ω scan and 2θ scan are needed in the alignment process, and coupled scan is usually used to show the final result.

The diffraction planes can be classified to be symmetric planes and asymmetric planes. The angle between diffraction plane and incident angle is ω , while the diffracted angle is 2θ . Symmetrical planes are the planes that are parallel to the surface of the sample, while asymmetrical planes are the planes that have an angle to the surface of the sample (obtained by tilting the sample). Symmetrical and asymmetrical scans are both needed to be able to investigate different properties of materials. Symmetrical scans only provide information about in plane (parallel) lattice parameter. Among these planes, mostly c -directed symmetric (002), (004), and (006) planes are scanned. But (102), (111), and (121) are asymmetrical planes. Symmetrical plane measurement was used to find the tilt of the epitaxial layer, while asymmetrical plane measurement was used to find lattice mismatch, strain, and relaxation. Also, c -lattice length is determined from symmetric plane peaks, and a -lattice length is determined from asymmetric plane peaks. For example, while examining GaN layer, symmetric scans for these planes can be made. χ and φ axes are also used with ω and 2θ axes for (102), (111), and (121) asymmetrical planes. In this kind of analysis, ω , 2θ and χ values of crystallographic asymmetric planes or tilt angle should be determined with a software or by using vector operations. After calibrating these values on the device, φ scanning is made. After calibration of φ , determined from scanning peaks, sample is scanned in 2θ angle from right and left. For example, $\pm(1, 2$ and $3)$ degrees.

For example, Fig. 12a shows a coupled scan plot, in which intensity is plotted against 2θ , and ω is changing. The figure shows the $\omega - 2\theta$ scans of $\text{Al}_x\text{Ga}_{1-x}\text{N}/\text{GaN}$ ($x = 0.3$) structures with and without a high-temperature AlN interlayer and AlN buffer layer on sapphire substrates for the three high-electron mobility transistor

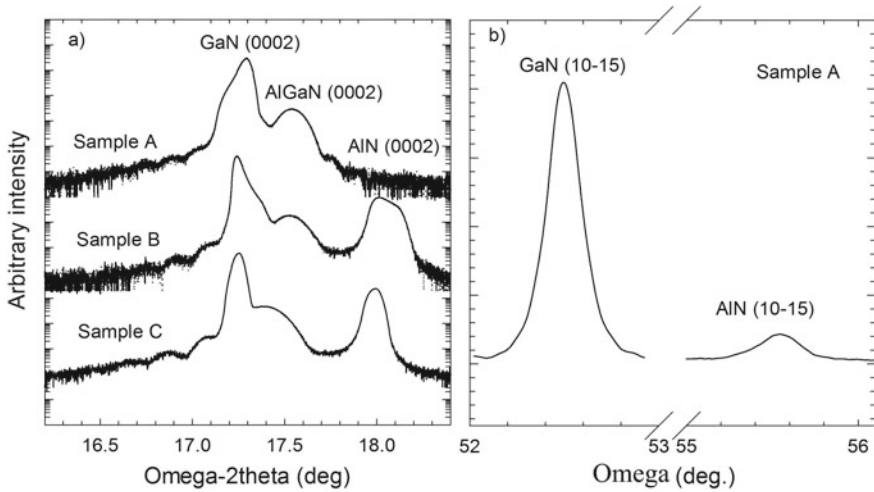


Fig. 12 a High-resolution Bragg reflections near the (0002) reflection of samples A, B and C. b The (10 $\bar{1}5$) rocking curve of the GaN layers and the AlN interlayer in sample A [36]

(HEMT) samples [36]. As shown in Fig. 12a, besides the AlGaIn (0002) and AlN (0002) reflections, an intense GaN (0002) reflection along with its strong interference with AlGaIn was observed, in turn indicating that the GaN, AlN, and AlGaIn layers possess high-quality wurtzite structures. Here, miller planes of hexagonal structure are indicated by $(hk(-h-k)l)$. In the skew geometry of XRD, the ω peak of the asymmetric (10 $\bar{1}5$) plane in the interlayer was the only one found and was shown by the ω scan of the GaN (10 $\bar{1}5$) reflection, as shown in Fig. 12b.

Qualitatively, the determination of the quality of crystal can be taken based on the full width at half maximum (FWHM) of the peaks. A perfect crystal will have a very sharp peak. A broadening of the curve can be related to the presence of mosaicity, dislocation, or curvature in the sample. Plane quality is determined by fitting the ω turning peak half height width (FWHM) to the Gaussian function. The quality of the FWHM increases when approaching to the FWHM value of 0.00435° (15arcdeg) gained from silicon calibration of Ge monochromator.

4.2.5 X-Ray Florescence (XRF)

The mechanism of this technique is easy to understand if compared with XRD. In XRD, only K_α source spectra are used, but in XRF, all the spectrum coming from the tube is used which is called primary. In this technique, irradiation of a sample by bombarding with primary X-ray beam from an X-ray tube causes emission of fluorescent X-rays with discrete energies characteristic of the elements present in the sample. It can be seen in Fig. 10d that when the whole beam comes over the sample, in all types of atoms forming the sample, the electrons in inner shells like

K, L, and M are excited, and luminescence effect is seen. So, K_{α} , K_{β} , L_{α} and L_{β} spectras are seen for every element in the sample. The spectra of these elements are compared with database, which was prepared for all elements, and constituent elements of the sample under study are determined. This determination should be made before the compound determination in XRD. It is useful to know the atoms forming this compound in XRD.

Analysis is made using one of two spectrometers of two design principles: wavelength-dispersive X-ray fluorescence spectrometers (WD-XRF) and energy-dispersive X-ray fluorescence spectrometers (ED-XRF). WD-XRF spectrometer uses a crystal monochromator as a grating to diffract the fluorescent X-rays to produce a spectrum. So, just a single wavelength at a time is received by the detector that measures their intensity. But the ED-XRF spectrometer permits the fluorescence radiation of all wavelengths emitted to reach the detector simultaneously, and it uses a pulse height discriminator to classify the energy of the X-ray photons that strike the detector.

All the elements till uranium can be analyzed by this technique. Geological and underground good samples are commonly examined with XRF technique. Especially for underground investigations, there are portative XRFs put in a bag or shaped like a gun. A historical self-portrait painted by Sir Arthur Streeton (1867–1943) has been studied with fast-scanning X-ray fluorescence microscopy using synchrotron radiation given in Fig. 13 figured by Hovard et al. [37]. Also, XRF technique is commonly used in the powder analyses with XRD [38].

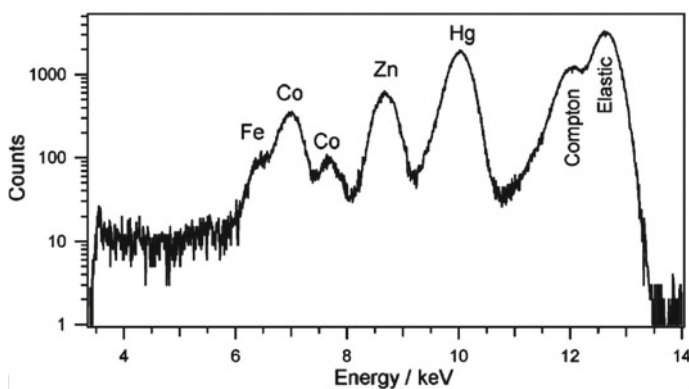


Fig. 13 Representative X-ray fluorescence spectrum of a 50 mm² area of the painting near the chin collected by 1 of the 384 detector elements of the Maia detector array. Several major elemental fluorescence lines and the scattering components are labeled [37]

4.3 Secondary Ion Mass Spectroscopy (SIMS)

In this technique, an ion gun is used to produce a precisely focused energetic primary ion beam (typically between 25 and 30 keV kinetic energy) that sputters the surface of the sample. Because of this primary ion sputtering, a collision cascade is induced in the upper surface layers of the sample. Due to energy dissipation resulting from these collisions, bonds will be broken and secondary particles will be emitted. The emitted secondary ions (positive or negative) are collected and analyzed by mass spectroscopy, where they are separated from each other according to their charge and mass ratios. Three types of signals are taken from the scattered ions. These are ion images, depth profiles, and mass spectra, respectively. So, 3d mapping of the elements and molecules can be made. As an example, SIMS depth profile of gallium-doped zinc oxide (GZO) thin films which were successfully deposited onto n-Si and glass substrates by RF magnetron sputtering at room temperature using a power of 200 W [39] is presented in Fig. 14. Ga and Zn homogeneity in the layers give very good results.

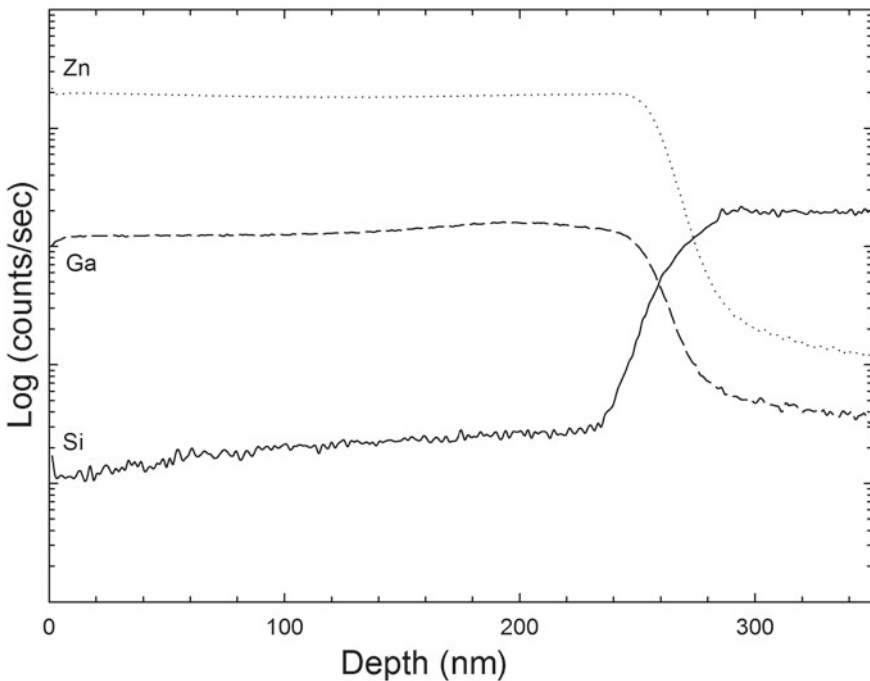


Fig. 14 SIMS depth profile of GZO thin films onto n-Si and glass substrates [39]

4.4 Stress Measurements

In stress measurements, there are two modes: the “iso inclination” and the “side inclination.” In the iso-inclination mode, the 2θ is measured by aligning the χ plane (the plane that connects the normal of the sample surface to the normal on lattice plane) to the detector scanning plane (2θ scan). In the side inclination mode, the 2θ is measured by setting the detector scanning plane perpendicular to the χ plane. This mode permits the use of large values of the angle χ to measure the bottom or curved sections of a gear, which are difficult to measure by the iso-inclination method.

Using XRD and Bragg’s law, stress measurements can be performed for semiconductor and metal material by measuring detector angle 2θ while varying the angle χ , where χ is formed by the normal of the sample surface and the normal to the lattice plane. In these measurements, if there is stable stress in any direction, the diffraction peak of this direction is used. Setting the angle of the X-ray beam at fixed value, the value of d at the position of the diffraction peak can be found by substituting $n = 1$ in Bragg’s law, $2d \sin(\theta) = \lambda$. For a symmetric and asymmetric peak in the ω scans, the peak will be determined through scanning in a narrow range. The value of d and data corresponding to changing χ value is used the stress equation;

$$d = d_0 \frac{1 + \nu}{E} \sigma \sin^2(\chi) - d_0 \frac{\nu}{E} (\sigma_{11} + \sigma_{22}) \quad (8)$$

According to this equation, the plot of d versus $\sin^2(\chi)$ will be linear. So, by performing a linear fit, and using the slope m obtained from the fit, the stable stress can be calculated from the formula:

$$\sigma = \frac{m}{d_0} \frac{E}{1 + \nu} \quad (9)$$

where Young’s modulus E , Poisson ratio ν , and lattice spacing in stress-free conditions d_0 are known for the material. As an example, d versus $\sin^2(\chi)$ curve is given in Fig. 15 for Ge semiconductor. χ angle is taken between 0 and 4° with steps of 0.1° for stress measurements by using side inclination mode. By using symmetric (004) ω -scans we find d of the peak with the help of Eqs. (8) and (9) as mentioned above.

Stress curve is plotted. The equation of the regression straight line is found from the plot as: $y = -0.0004x + 1.3663$, where $x = \sin^2(\chi)$. Using the slope of the straight line, which is $m = -0.0004$, Young module, for Ge $E = 150$ GPa, Poisson ratio $\nu = 0.3$, and universal $d_0 = 1.3577$ values, the stable stress was calculated and found to be -34 MPa.

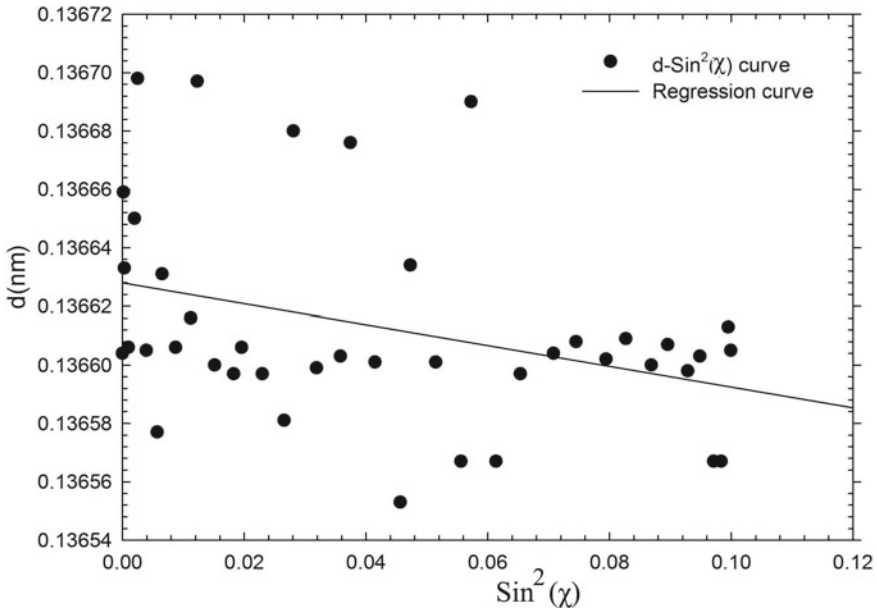


Fig. 15 d versus $\text{sin}^2(\chi)$. plot for Ge semiconductor

4.5 Texture Calculation

In this method as in XRD, $K_{\alpha 1}$ and subdued $K_{\alpha 2}$ spectral peaks are used. Generally, pinhole apparatus is used, and pole images are made. Primarily in a textured material, diffraction peaks should be seen, and when the Bragg condition is maintained with θ , the range giving the d values is kept constant. After this, diffraction peaks are tried to be seen again and again with Cradle attachment and χ tilt and ϕ turn angles in a certain range. After this, for analyzing the data peak intensities which have d values gained from every χ (tilt) and ϕ (rotation) angle scans, three-dimension pole (χ , ϕ , and intensity) is plotted. Texture mapping can be given as an example to this situation. In texture analysis, as standard measurement ranges, 2θ range is $2.5\text{--}70^\circ$, χ tilt angle range is $0\text{--}85^\circ$ or $0\text{--}350^\circ$, and ϕ turning angles can be used in every 6-degree steps. Pole graphs need wide data analysis because of fingerprints of the X-ray beam by sintonization detectors. Texture analysis became more convenient with fast pixel detectors. In texture analysis, spreading of the lattice plane direction is shown in a half sphere. Sample may be weak, heavy, and normal texture. In investigations, direction of a plane can be determined with 2θ scan without using pole graph. In the degree of direction, texture percentage of crystal lattice plane is determined by the ratio of single peak area to total area of peaks.

4.6 *Small and Wide-Angle X-Ray Scattering (SAXS and WAXS)*

Small-angle X-ray scattering (SAXS) is an analytical technique that measures the intensities of X-rays scattered by a sample as a function of the scattering angle. Measurements are made at very small angles, typically in the range of $0.1\text{--}5^\circ$. A SAXS signal is observed whenever a material contains structural features on the length scale of nanometers (1–100 nm). SAXS method is one of the most versatile techniques for the structural characterization of nanomaterials. The samples may be solid objects, powders, gels, or liquid dispersions, and they may be amorphous, crystalline, or semi-crystalline. SAXS also gives knowledge about the structural dynamics. Measurements can often be done in situ, and only, minimal sample preparation is required. It is essential to use a detector which has a high linearity, a high dynamic range, and negligible intrinsic noise. For high-end SAXS instrumentation, a high spatial resolution of the detector is beneficial.

Wide-angle X-ray scattering also known as wide-angle X-ray diffraction (WAXD) is the same technique as small-angle X-ray scattering (SAXS), except that the distance between the sample and the detector is smaller, and thus, diffraction maxima at larger angles are observed for WAXS. Wide-angle X-ray scattering (WAXS) probes the material for the much smaller length scale (interatomic distances). It is used to determine the crystalline structure of polymers and to determine the chemical composition, phase, or texture of films. Wide-angle X-ray scattering can be measured simultaneously with SAXS.

Small-angle X-ray scattering and wide-angle X-ray scattering (SAXS and WAXS) are complementary techniques. WAXS usually covers angular $5\text{--}60^\circ$, while SAXS covers much smaller range, which is up to 5° . WAXS and SAXS methods do not harm the sample. As an example, spherical polyelectrolyte brushes analysis with SAXS is given in Ref. [40].

4.7 *Atomic Force Microscopy (AFM)*

AFM is a very high-resolution scanning probe microscope, with a resolution of fractions of Angstrom. It is used widely for examining organic and inorganic sample surfaces. It is in the first plan for examining structural properties of surfaces of optoelectronic devices. AFM contains a cantilever with a sharp tip (probe) at its end that is used to scan the specimen surface at the nanoscale level. Fundamentally, it depends on the interaction of the tip with atoms (Fig. 16). AFM has three different modes. These are contact mode, where the tip touches the surface of the sample; noncontact mode, where the tip does not touch the surface; and the tapping mode, where the tip hits the sample surface. Tips are made of different materials for different aims. Tips are made of Si, Si_3N_4 , Au, and Pt, or other molecular materials coated with them. For this reason, in each mode, different tips are used. Here, forces coming out from

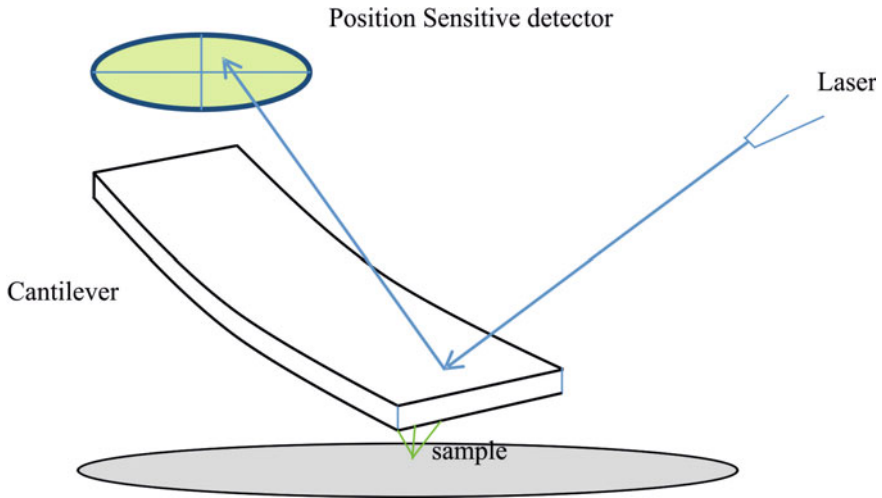


Fig. 16 Schematic of atomic force microscopy (AFM)

Wan der Waals interaction ($F = kz$) transforms to motion on the tip made up of Si_3N_4 and SiO_2 materials. This motion transforms to data with the help of a photodiode which makes laser trace. While the tip is approaching to the surface pulling and pushing, Wan der Waals interacts and a resonance period starts. Roughness, friction, electrical properties, magnetic properties, nanomechanical properties, and corrosion can be determined about the sample.

Surface images of the $\text{AlInN}/\text{AlN}/\text{GaN}/\text{Al}_2\text{O}_3$ HEMT (high-electron-mobility transistor) structures grown by MOCVD with various thicknesses of GaN top layer and AlInN layer having different indium compositions are given in Fig. 17 [41], where the scan area of the AFM images of GaN top layer of the samples is $4.0 \times 4.0 \mu\text{m}^2$. The thickness values of the buffer AlN layer for samples A, B, and C are 14.0, 8.0, and 14.0 nm, respectively, and for GaN, cap layer are 1.0, 2.0, and 4.0 nm

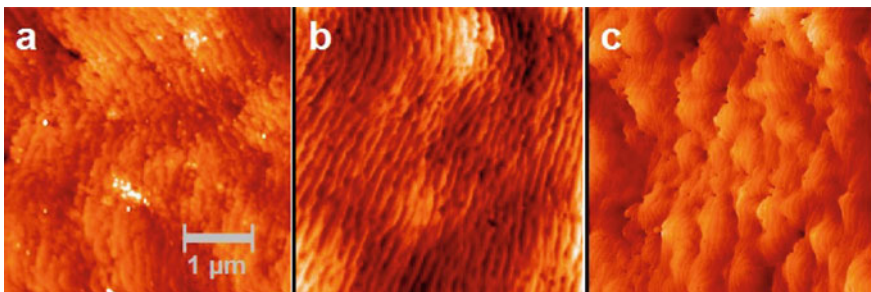


Fig. 17 AFM images of AlInN/AlN/GaN heterostructures with different AlN Buffer Thickness [41]

for samples A, B, and C, respectively. As it is clearly seen in these images, surfaces are similar and are composed of steps and terraces.

Notwithstanding the pure atomic steps that are commonly seen in sample C, the black points, which are typical for GaN surfaces [42–46], still appear on the surface image of the top layer. The average root mean square (RMS) roughness of samples A, B, and C was attained as 0.450, 0.270, and 0.570 nm in a scan area of $4 \times 4 \mu\text{m}^2$.

Lattice mismatch between sapphire and AlN increases the dislocation density in the AlN layer, and dislocation is carried to the surfaces causing cracks. In this case, the nucleation of AlN and GaN interlayers can be grown to prevent surface cracking. As a result, the surface morphology looks good [43].

4.8 Spectroscopic Ellipsometry (SE)

Ellipsometry method is widely used for the examination of the films over substrates for measuring the optical activity in surface investigations [47], where optical activity of the films is known as polarimetry. It is also used for determining the thickness of unknown films, optical properties of materials, and surface density of overlayers on reflective materials. But it must be noticed that materials properties and other physical parameters determined by ellipsometry are inherently dependent on the physical model assumed by the user. SE method is a harmless method for determining optical properties of semiconductors, metals, and insulators. It is also used for determining the boxing of the reflected light from the surface of the film [48].

Ellipsometry in general makes use of the fact that the polarization state of light may change when a light beam is reflected from the surface of a sample. Ellipsometry analyzes this change of the state of polarization and yields information about the layers of the thin film that are often even thinner than the wavelength of the probing light. A basic ellipsometer consists of a source of light, a polarization state generator (PSG) placed in the path of the beam before the sample, a polarization state analyzer (PSA) placed in the path of the beam behind the sample, and a photo detector. The PSG controls and analyzes the polarization state of the probing light, while the PSA controls and analyzes the polarization state of the reflected. There many different types of PSGs and PSAs exist. In ellipsometry, the probing beam hits the sample under an oblique angle of incidence. Consequently, the phase change caused by the probing beam to the reflectivity of the sample is different for light with polarization parallel and perpendicular to the plane of incidence, respectively (p- and s-polarizations). Ellipsometry measures both the ratio of the reflectivity and the relative phase change of the p- and s-components and yields the ellipsometric angles ψ and Δ :

$$\tan \Psi = \frac{|R_p|}{|R_s|} \quad (10)$$

$$\Delta = \Delta_p - \Delta_s \quad (11)$$

Table 3 Solar cell structure

n-GaAs Cap layer 50 Å
n-GaInP 2000 Å
p-GaInP 2000 Å
p-GaAs 150 Å
n-GaAs 150 Å
n-GaAs 2000Å
p-GaAs buffer layer 3000 Å
3'' p-GaAs (100) substrate

where R_p and R_s are reflectivity of p- and s-components, respectively, while Δ_p and Δ_s are the induced phase change on these p- and s-components, respectively. By using ellipsometric equations, ellipsometric ratio is calculated by the following formula;

$$\rho = \left| \frac{R_p}{R_s} \right| = e^{i(\Delta_p - \Delta_s)} = \tan \psi e^{i\Delta} = \frac{R_p}{R_s} \quad (12)$$

These equations are fitted with suitable models based on Fresnel equations with ellipsometric data, so they give the optical parameters of the solid material [49]. With this SE method, primarily, refractive index, film thickness, extinction coefficient, and crystallite and alloy ratio can be determined.

SE analysis for the $\text{Ga}_{0.516}\text{In}_{0.484}\text{P}/\text{GaAs}$ solar cell structure (Table 3) was measured at an angle of incidence 70° by Kinaci, et al. [50]. Figure 18a shows the real and imaginary parts of the dielectric function against photon energies in the range 0.6–4.7 eV. It should be noticed that (E_0 , $E_0 + \Delta_0$, E_1 and $E_1 + \Delta_1$) in Fig. 18a are the critical point energies. We have calculated numerically the second derivative spectra of the real part of the experimental dielectric function to perform the line–shape analysis, which was given in Fig. 18b. The experimental curves were fitted to determine the critical point energies. So, E_0 , $E_0 + \Delta_0$, E_1 and $E_1 + \Delta_1$ were found as 1.92, 2.05, 3.25, and 3.45 eV, respectively [50].

4.9 Photoluminescence Spectroscopy (PL)

Photoluminescence spectroscopy (PL) is an optical method used in characterization of materials. In this technique, sample is exposed to electromagnetic radiation and the energy is absorbed and the material is transferred to a higher energy state. The release of energy through the emission of radiation during relaxation of the material to return to lower energy states is called photoluminescence (PL). PL is a very simple method, where the intensity of the incident wave and spectrum can be determined very fast, and it does not deform, or heat the sample. PL may be used in determining doping ratio of III–V group semiconductors, structural defects, and band

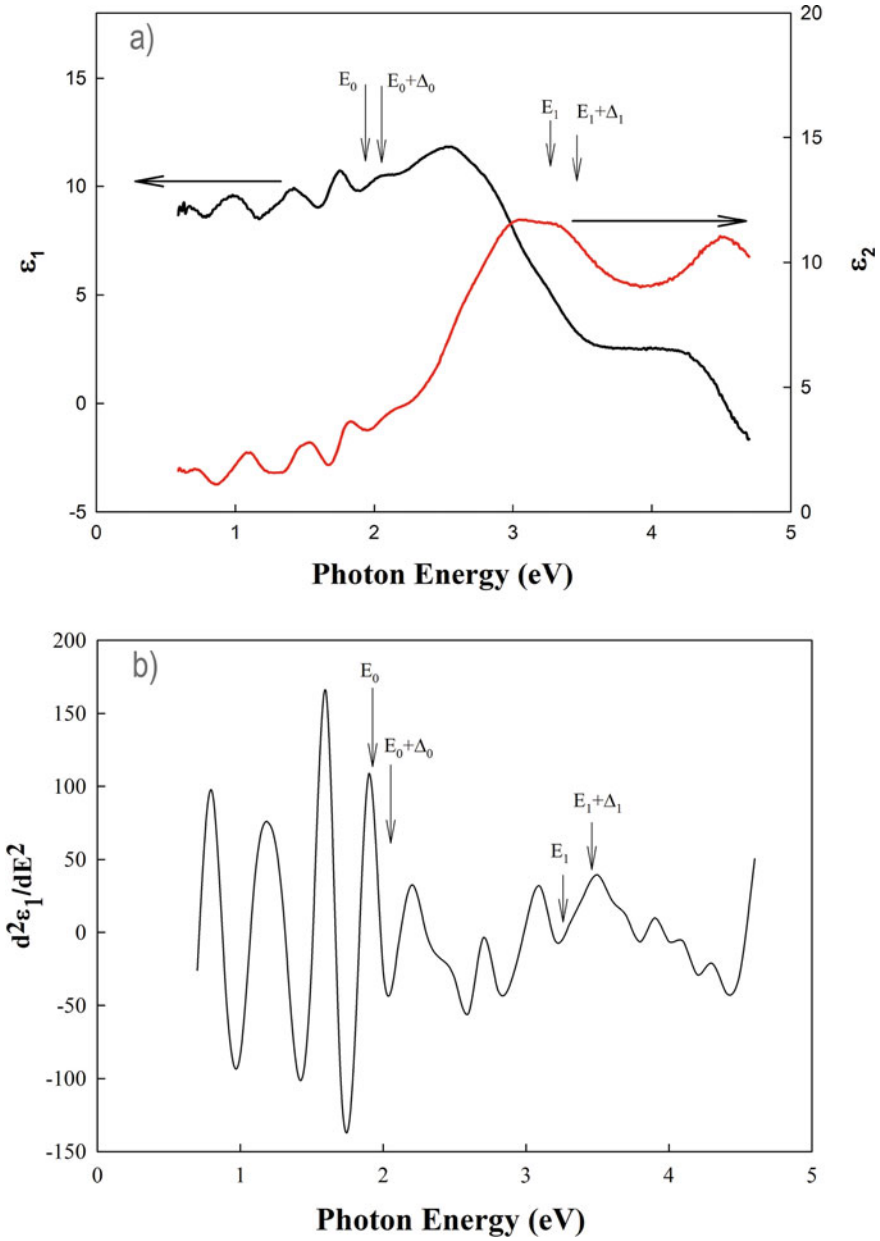


Fig. 18 **a** Real and imaginary parts of the dielectric functions of $\text{Ga}_{0.516}\text{In}_{0.484}\text{P}/\text{GaAs}$ solar cell structure. **b** the second derivative spectra of the real part of dielectric function spectrum of $\text{Ga}_{0.516}\text{In}_{0.484}\text{P}/\text{GaAs}$ solar cell structure [50]

gap. Intensity and spectral property of PL give knowledge about different properties of the sample [51]. It is an efficient method in determining forbidden band gap and different behaviors. PL is sufficient in determining forbidden band gap at room temperature in helium atmosphere; even it is more stable, for project studies. When producing LED, detector, and photodetector, it is a routine spectrum technique [52]. By using PL measurements, it is possible to control conditions which come out with surface variations. It gives optical knowledge about deformed region near to surface under high pressure. It can examine optical behaviors of interfaces. Surface area of the sample which is exposed to PL may decrease the PL intensity. According to other spectrum devices, sample surface roughness or structural irregularity is also not limiting [53]. In semiconductor materials which have indirect band gap, the PL has less efficiency. Irradiative transitions cause relaxation of excited populations in these samples. This situation may increase population because of structural defects such as surface oxidation. For this reason, fast and irradiative excitations may occur. PL peak may be seen even in this condition. This peak may be characterized with both radiative and irradiative excitations. With PL, it is not possible to determine irradiative traps directly. But the traces of these traps may be seen clearly in some measurement types of PL. It is a difficult investigation to examine interface and doping conditions by using PL spectrum. If the mentioned situations are radiative mechanism situations, they can be examined in PL spectrum and the size of the corresponding PL peaks permits to examine the doping condition of the sample. But it is difficult to measure the density of these levels, and it is exhausting that the exciting intensity of PL peaks is in ratio [52].

As an example, the PL measurements of hetero-junction GaAs and solar cell are taken at 300 K (room temperature), and it is shown in Table 4 as an example. Forbidden band gaps and alloy ratios(x) of semiconductor materials forming GaAs solar cell are gained from PL spectra peak positions. PL intensity versus wavelength plot is given in Fig. 19 for hetero-junction GaAs solar cell structure. Forbidden band gap of GaAs semiconductor material is calculated as 1.42 eV by using these peak positions. $\text{Al}_x\text{Ga}_{1-x}\text{As}$ window layer's forbidden band gap is found as 1.865 eV. Aluminum composition ratio in $\text{Al}_x\text{Ga}_{1-x}\text{As}$ alloy is found as %36.00 by the help of forbidden band gap [54].

Table 4 Schematic view of hetero-junction GaAs solar cell grown at 300 K

p+GaAs (Cap) 20 nm
p-AlGaAs 30 nm
p-GaAs 500 nm
n-GaAs 500 nm
n + GaAs (buffer)
3" n-GaAs (100) substrate

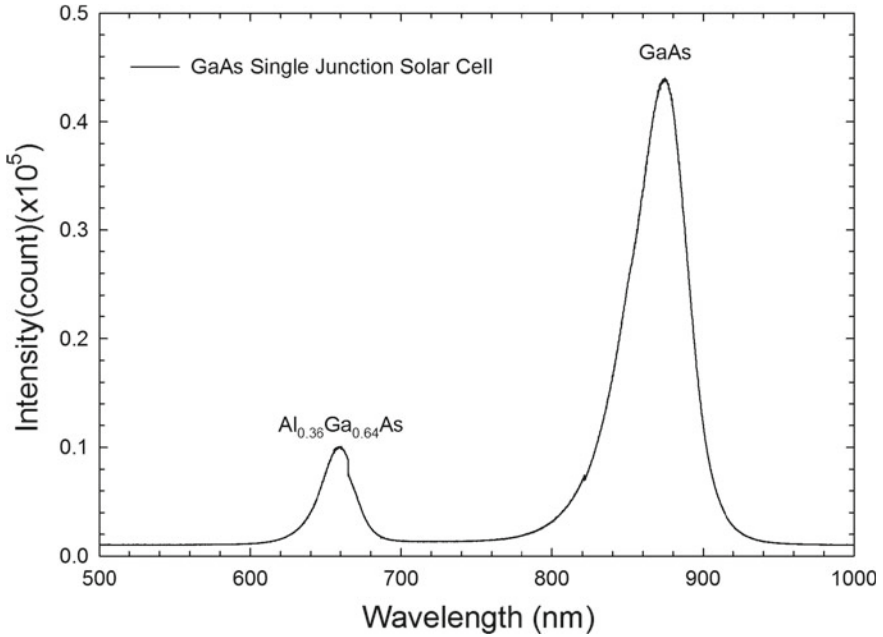


Fig. 19 PL intensity versus wavelength for hetero-junction GaAs solar cell

4.10 Raman Spectroscopy

At the beginning of twentieth century, first, Raman spectroscopy was performed for determining solutions and organic materials by Raman [55]. The measurements gained by the help of this method can be taken by not deforming the material. Raman spectroscopy method is used as material characterization by the vibrations belonging to the material. In the middle of the twentieth century, it is started to be used commonly in semiconductor technology. When a monochromatic light beam (usually laser beam) excites a material, most of the scatters over the material come out elastically. In these scatterings, no energy variation is seen among atoms and molecules. For this reason, the incident electromagnetic radiation scatters in the same wavelength. Scattering in this wavelength may be seen together with less intensity of non-elastic scattering. When the energy difference between incident and scattered light is investigated, it is observed that the energy of inelastic scattered light is different from material to material [56], which means that vibrational energies differ from material to material or each material has its fingerprint. If the scattering is elastic [57], there is no difference in the energy between incident and scattered photons, and it is called Rayleigh scattering. If the scattering between the molecule and the photon is inelastic, it is called Raman scattering.

Vibrational energy after the collision and the wavelength of the inelastically scattered photon are inversely proportional with each other. Momentum and total energy

are conserved during scattering. After inelastic scattering, the molecule moves to a new energy state, and the scattered photon shifts to a different energy, or to a different frequency. The energy difference of the scattered photon equals to the energy difference between the initial and final energy states of the molecule. If the final energy state of the molecule is higher than the initial one, or in other words the vibrational energy of the molecule increased after the collision, then the scattered photon will be shifted to a lower frequency (lower energy) and that the total energy of the system remains constant. This shift in frequency is called a Stokes shift, or downshift. If the energy of the final state of the molecule is lower than the initial state, or in other words the vibrational energy of the molecule decreased after the collision, the scattered photon will be shifted to a higher frequency, which is called an anti-Stokes shift, or upshift, and in this case, the molecule should be excited [56, 58].

Some positive and negative aspects of Raman spectra:

- (a) Compleitive data may be gained by different adjustments.
- (b) It is easy to apply.
- (c) It does not require material preparation.
- (d) Experimental procedure may continue repeatedly.
- (e) Adding some noise to the spectrum may cause complications.

Raman spectra of the high-resistivity GaN epilayers are given in Fig. 20a grown on 6H-SiC substrate with different buffer structures which were recorded at room temperature [26]. As shown in Fig. 20a, in the back-scattering geometry measurements, the allowed E_2 (high) and the A_1 (LO) phonon modes of the c-direction-oriented GaN and the E_2 (TA), A_1 (LA), E_2 (TO), and A_1 (LO) phonon modes of the 6H-SiC substrate can be fitted as Ref. [59]. In Fig. 20b, GaN E_2 (high) and A_1 (LO) mode's Raman spectras are seen separately [26].

For a detailed Raman analysis, a second sample can be given. Raman spectra for samples A and B of details in Table 5 are shown in Fig. 21, where spectra are gained using micropublisher 5.0 camera software. During these measurements, the 785 nm wavelength laser is used for 60 s for both samples.

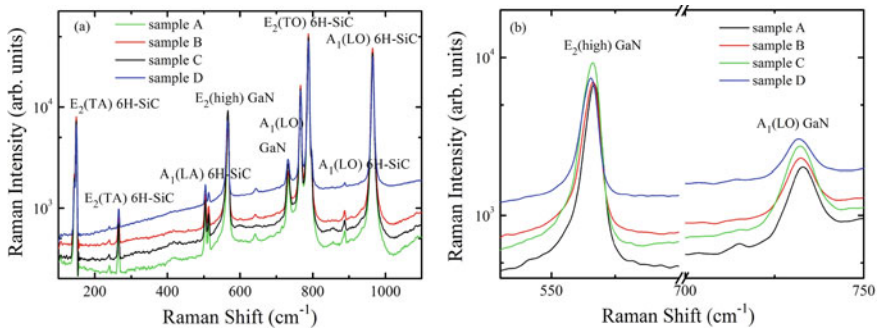


Fig. 20 **a** Raman spectra obtained at $T = 300$ K for the HR-GaN epilayers grown on 6H-SiC substrate with different buffer structures, for back-scattering (surface) geometry ($\vec{z}(x, x)z\vec{z}(x, x)z$). **b** E_2 (high) and A_1 (LO) phonon modes in the HR-GaN epilayers [26]

Table 5 Schematic diagram of (a) Sample A and (b) Sample B [60]

Sample A	Sample B
p-InGaN layer 20 nm	p-InGaN layer 20 nm
p-InGaN layer 50 nm	p-InGaN layer 50 nm
Graded InGaN layer 25 nm	–
p-InGaN layer 200 nm	InGaN layer 220 nm
n-GaN layer 1.9 μm	n-GaN layer 1.9 μm
Ud-GaN layer 1.9 μm	Ud-GaN layer 1.9 μm
LT-GaN 2.45 min	LT-GaN 2.45 min
4H-Al ₂ O ₃ substrate	4H-Al ₂ O ₃ substrate

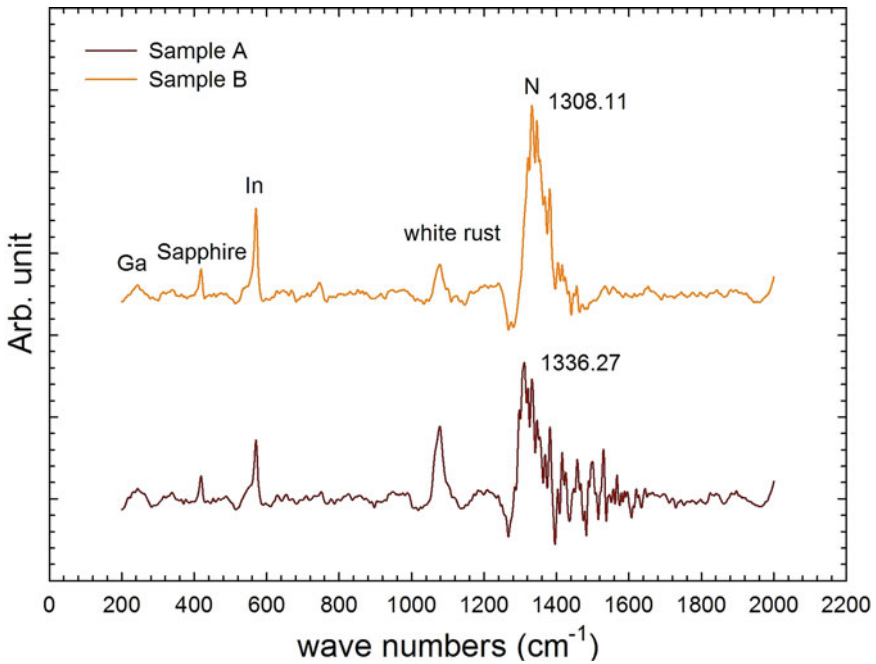


Fig. 21 Raman spectras for Sample A and B [60]

Raman spectra can be used for determining, crystallite size, identification of material, and stress. In Table 6, one can see the results for peak center, peak height, peak area, and full width at half maximum values (FWHM) values for InGaN/GaN structure. There is also one more layer detected by Raman measurement that is white rust formed by touching the air for a long time.

Amount of materials in the samples are estimated by peak intensity ratio and peak area ratios that are shown in Table 6. Crystallite size can be estimated using FWHM data in Raman spectra. Atomic radius of materials can be calculated by

Table 6 Raman analysis data for two InGaN LED structures

	A					B				
	Ga	Al ₂ O ₃	In	N	White rust	Ga	Al ₂ O ₃	In	N	White rust
Peak center	244	419	571	1336.27	1078	244	419	571	1308.11	1078
Peak area ratio(%)	3.28	1.95	8.20	17.60	3.24	3.21	2.62	9.47	17.39	6.92
Peak height ratio(%)	2.22	5.83	10.74	76.03	5.16	5.82	7.98	18.89	45.53	21.76
FWHM	34.09	8.91	12.48	26.69	–	33.83	9.54	10.65	25.37	–

equation $r = r_0 \cdot A^{1/3}$ [61], where r is the atomic radius, A is atomic number, and r_0 equals 1.2 fm. If FWHM values of Ga and N are compared with their atomic radii, it is seen that they are in good agreement. FWHM values of sample A are generally bigger than those of sample B. This means that crystal quality is better for sample A. As mentioned before stress can be calculated from Raman spectra. During the calculation of stress values, unstressed peak center values must be found from RRUFF database. These values are subtracted from experimental values and divided by calibration coefficients to gain stress in MPa. This relation is shown with equation $\sigma(\text{MPa}) = \Delta w(\text{cm}^{-1})$ [62].

In Raman calculation, N peak center value is used because it is the most intense peak in both samples. Stress values from Raman are calculated as 4.27 and -23.89 Mpa. There is one more layer detected by Raman that is white rust ($3\text{Zn}(\text{OH})_2\text{ZnCO}_3\text{H}_2\text{O}$). Peak intensities of white rust are different in both samples, which is related to different cleaning durations.

4.11 *Fourier Transform Infrared Spectroscopy (FTIR)*

FTIR spectroscopy is related to the measurement of interatomic bond vibrations of the (IR) absorbing material. IR spectrum is modulated with strain, shrinkage, and twist bonds in the structure. Modulation of positions in these interatomic bond vibrations is taken into resonance with unstable positions in IR region. Every functional group has its own vibrational frequency and spectrum [63].

IR spectroscopy is a fast and simple technique for determining different functional groups. As in all spectroscopic methods, IR spectroscopy is also dependent on the interaction of atoms or molecules with electromagnetic radiation. Infrared (IR) spectroscopy is the technique to explain inorganic, organic, and biological structures [64–67]. Shortly, IR spectroscopy is the technique, which is used for measuring vibrational spectra, that is absorbed in a wide range dependent on wavelength. IR measurements can be done using transmission or reflection [68], but transmission situation is more common. The wavelength range of IR spectrum is between 0.78 and $1000 \mu\text{m}$ ($12500\text{--}10 \text{ cm}^{-1}$ wave number). This may be grouped as far IR ($100\text{--}10 \text{ cm}^{-1}$), middle IR ($4000\text{--}100 \text{ cm}^{-1}$) [69, 70], and near IR ($12500\text{--}4000 \text{ cm}^{-1}$) [71]. Near and middle IR are the most commonly used regions [59].

IR rays cause atoms to vibrate with an increasing amplitude around bonds connecting atomic groups. IR light does not have sufficient energy to excite electrons as ultraviolet or high-energy radiations do. Because functional groups of organic molecules are formed by ordering of connected atoms belonging to functional group, absorption of IR energy by organic molecules comes out typically by atoms found in determined functional groups. Vibrations coming out like this are the vibrations, which are quantized by the absorption of IR energy by compounds. The position of an IR absorption band is measured as the reverse of the centimeter (cm^{-1}), and it is indicated by wave number (ν) or wavelength (λ). Wave number is the vibration number of the wave in a unit length, while the wavelength is the distance between two tops of these vibrations. It is given by $\bar{\nu} = 1/\lambda(\text{cm})$ or $\bar{\nu} = 10.000/\lambda(\mu\text{m})$.

Vibration of covalent bonds resembles tiny springs, which hold atoms together. Atoms may vibrate as they are adjusted in certain frequencies. Excitation of the molecule from one vibrational energy to the other happens by absorption of IR rays at a certain energy (because $\Delta E = h\nu$).

Molecules may vibrate in two different types. These are;

1. Strain vibrations
 - a. Symmetric strain; atoms at two sides of the bond approach and get further at the same time.
 - b. Asymmetric strain; one of the bonds gets longer and the other gets shorter at two sides or just the inverse of this.
2. Bending vibrations
 - a. Inplane bending (shearing, shake)
 - b. Out-of-plane bending (twist, shake front, and back)

Strain frequencies in IR spectra may have two reasons. These are masses of the bonded atoms (heavy atoms have less vibrational frequency if compared with light ones), and the hardness of the bond. Triple bonds vibrate at higher frequencies than double bonds, and they are harder. The same relation is present between mono and double bonds. IR spectra of a compound are like its fingerprint. For this reason, if there are two different IR spectra, it is certain that they are different compounds. IR spectra of the same compounds are also the same [72]. Results in IR spectra are taken as absorption versus frequency plot.

In FTIR systems, no monochromator crystal is used. Spectrum is gained in time scale instead of frequency scale if all the frequencies interact with the sample. Data gained in time scale are named by interferogram. Interferogram is the Fourier transform of the absorption spectrum. Inverse Fourier transform operations are changed to data in interferogram frequency scale with the help of computer. Therefore, the well-known absorption spectra are obtained. Another function of the computer is gaining the spectrum in time scale many times, storing this data, and later measuring the total signal without noise. Here, a system called Michelson Interferometer is used [73]. FTIR spectroscopy is faster than IR spectroscopy, where the spectrum is registered in a few seconds. Sensitivity of the spectrum does not change because there are no solids and a high distorted spectrum is gained. Using FTIR spectroscopy, chemical bond and molecular structure of the top of a surface can be determined in a few microns. It is important to use IR spectroscopy in investigating organic materials with covalent bonds. These types of materials are analyzed in 2500-25000 nm wavelength range.

As an example, FTIR spectra for flash conductive-bridging random application, SiO₂ grown on Si/W and Cu doped SiO₂ films are given in Fig. 22 [74]. The Si–O–Si bonding and the Si–O bonding were observed at 1060 cm⁻¹, 835 cm⁻¹, and 461 cm⁻¹, respectively, in the SiO₂ film. For the Cu-doped SiO₂ film, there was additional Cu–O bonding appearing at 606 cm⁻¹ [74].

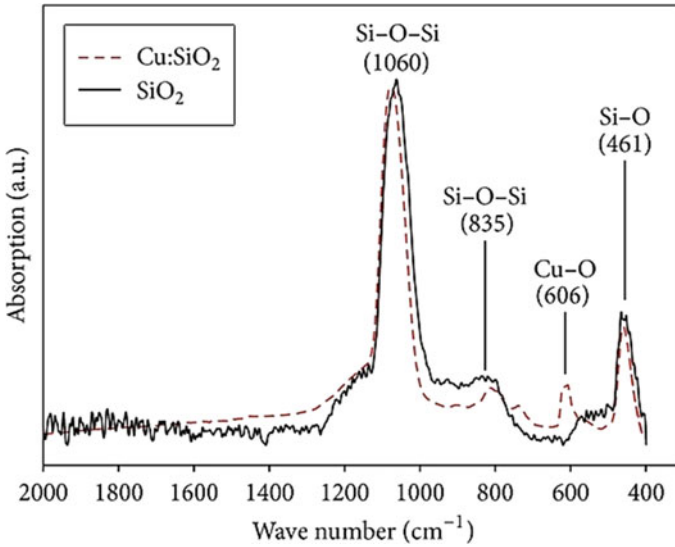


Fig. 22 FTIR analysis of the deposited SiO₂ and Cu:SiO₂ films [74]

4.12 Ultraviolet–Visible Spectroscopy (UV-Vis)

The principle of UV-visible spectroscopy is based on the absorption or reflection of ultraviolet or visible light of wavelength in the range 160–780 nm by a material, which results in the production of absorption spectra, and it depends on the interaction between light and matter. UV-Vis spectroscopy is mostly used for quantitative determination of molecules in a solution, or inorganic ions, or complexes. Most molecules absorb UV or VIS wavelengths, and a spectrum formed by absorption bands shows the structure of the molecule.

Charge transfer transitions among σ , π , and n molecular orbitals (both in organic molecules and in complexes) are seen. Also, there are transitions between d and f orbitals (in complexes) [75].

In organic compounds, it is difficult to examine excitations due to absorbing light at low wavelengths ($\lambda < 185$ nm). For this reason, vacuum is required for work on UV region. Electrons causing the absorption in organic molecules are electrons making bonds (electrons in bond orbitals π and σ) and electrons in non-bonding orbitals like sulfur, oxygen, nitrogen, and halogens which are found around atoms sharing electron pairs.

In thin film semiconductor structures, refractive index, energy band gap, and such optical coefficients can be determined by analyzing absorption and transmission spectra. Depending on the fact that a semiconductor material absorbs photons with larger energy than the forbidden band gap, and transmits the ones of smaller energy, it may be suggested that edge of the absorption spectra may correspond forbidden energy value.

Using the percent transmittance (T) measured with the spectrometer, the optical absorption coefficient of a thin film material with thickness d is determined by;

$$\alpha = -\frac{\ln(T)}{d} \quad (13)$$

In direct band gap semiconductors such as CdS and ZnO, the relationship between optical absorption coefficient and band gap energy is given as;

$$\alpha h\nu = B(h\nu - E_g)^{1/2} \quad (14)$$

Here, B is a constant, h is Planck's constant, ν is the radiation frequency, $h\nu$ is the energy of the incident photon, and E_g is the band gap energy [76]. Optical band gap of films may be determined by fitting the linear region of $(\alpha h\nu)^2$ versus $h\nu$ plot. By this method, when $(\alpha h\nu)^2 = 0$, the intercept point of the energy axis corresponds to the value of forbidden band gap energy. When the semiconductor material has indirect band gap, exponential term $1/2$ in equations is replaced by 2 [76].

As can be understood from the curve energy versus transmittance shown in Fig. 4.19 for n-type silicon, transmittance is about %90. Also, it is possible to measure forbidden band gap by using transmittance. For this operation, Tauc's plot is used given above. Changing of optical transmittance and $(\alpha h\nu)^2$ value versus photon wavelength/energy is given in Fig. 4.19. In this graph, x-axis intercept of the plot is known as forbidden band gap (Fig. 23).

Using Eq. (13), the absorption coefficient can be calculated from the transmittance. The plot of the absorption coefficient against radiation energy is given for n-type silicon in Fig. 24. In the plot, there can be seen a broad large peak with two smaller peaks. The position of the maximum peak for n-type silicon is seen around 2.33 eV.

UV-VIS can give wide optical data about the material. Using transmittance and reflectivity, the refractive index can be found. The following equations can be used;

$$n = \frac{\sum_{\lambda=\lambda_0}^{\lambda_m} \left(\frac{1 + \sqrt{(1 - T^2(\lambda))}}{T(\lambda)} \right)}{m} \quad (15)$$

$$n = \frac{\sum_{\lambda=\lambda_0}^{\lambda_m} \left(\frac{1 + R(\lambda) - \sqrt{R(\lambda)}}{1 - R(\lambda)} \right)}{m} \quad (16)$$

In these equations, m is the number of transmitters and reflectors for every wavelength value. Transmittance and reflectance spectra for of Corning glass are given in Fig. 25. By taking a certain λ value after the absorption edge, and using $T(\lambda)/100$ and $R(\lambda)/100$ at this selected wavelength, then substituting in Eqs. (15) and (16) given above, the refraction index is found as 1.530 from transmittance and 1.553 from reflectance. The difference between two situations is instability between 200 and 360 nm. It will be more suitable not to take this region.

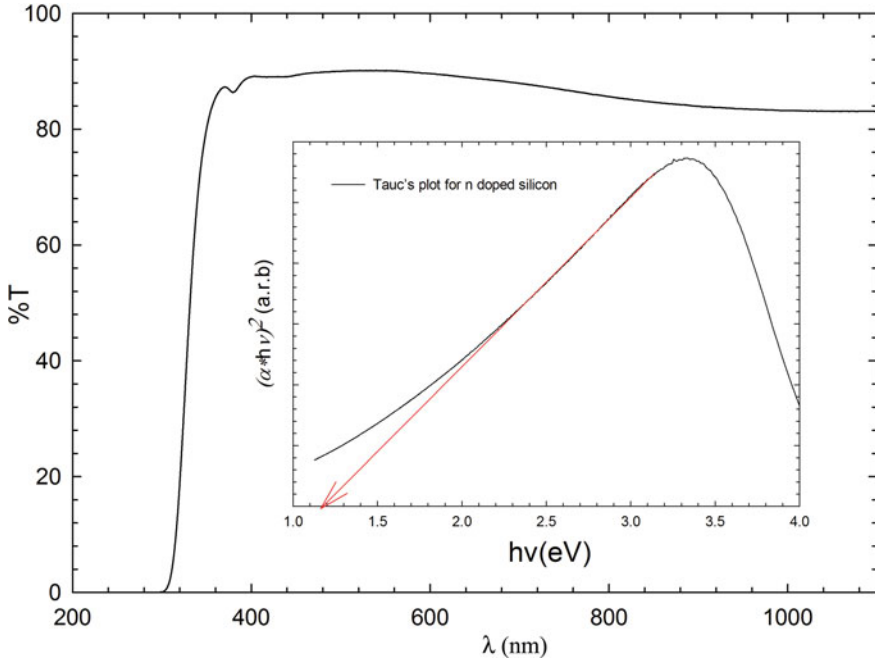


Fig. 23 Transmittance versus wavelength plot for n-type silicon, and $(\alpha hv)^2$ versus photon energy for silicon film (inset)

5 Conclusions

As a conclusion, there are ways to examine wide number of materials and their properties including every part of the electromagnetic spectrum with spectroscopy techniques. These techniques are developing continuously. Using spectral mapping, visualizing in 3D is an opportunity to improve characterisation. It is doubtless that development of nanotechnology is dependent on the development of these techniques. Besides, some of the questions that will be asked in the future are as “there is nanotechnology but why there is no Pico technology?” and qubit instead of 0 and 1 maintained by spin motions nowadays. That is 0 and/or 1 at the same moment, began to be mentioned for quantum computers for electronic bazaars. Although traditional devices are rapidly developing because their physics is not changing using frequency, bazaar percentage is too large. The life time of a device is changing between 15 and 30 years, because structural, electrical, and optical properties of the device are important, and these types of devices have become always popular.

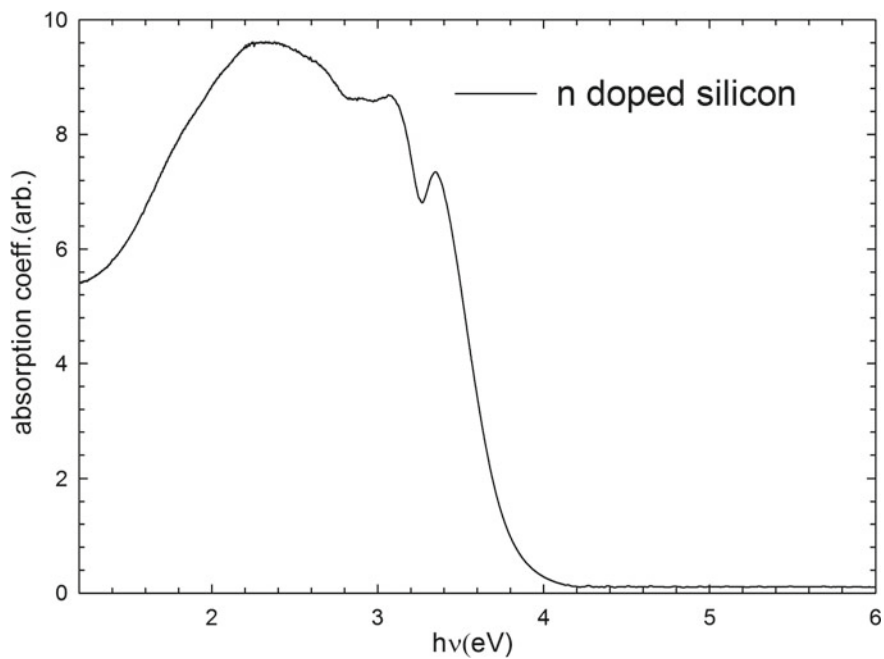


Fig. 24 Plot of the absorption coefficient against radiation energy for n-type silicon

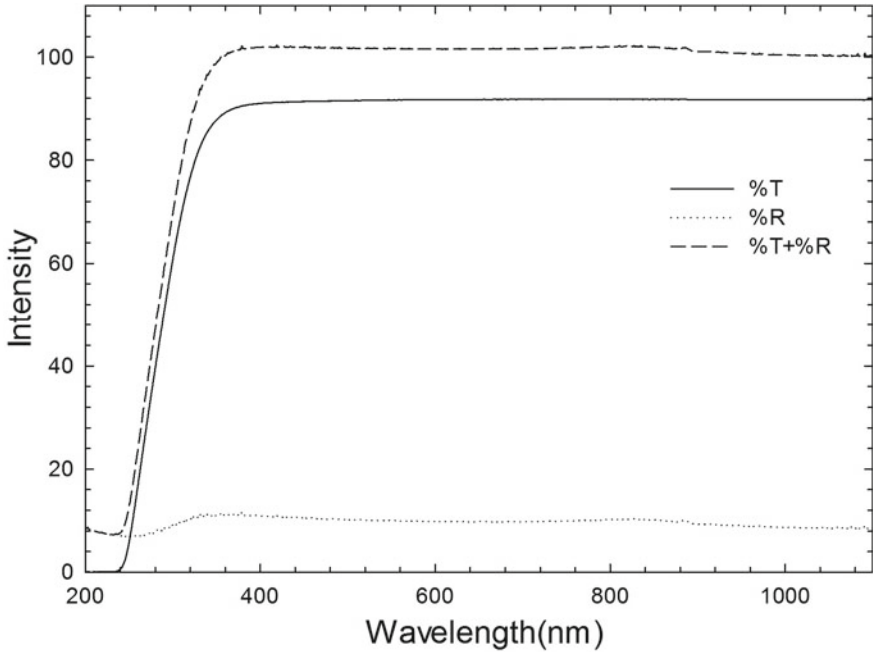


Fig. 25 Transmittance and reflectance spectra for Corning glass

Acknowledgements I would like to thank our many colleagues and also Director Prof. Dr. Süleyman Özçelik, Dr. Ömer Akpınar, Dr. Gürkan Kurtuluş, Dr. İlnur Kars, Dr. Nihan Akin Sönmez, Dr. Tuğçe Ateşer, and Dr. Neslihan Akçay, at Photonics Application and Research Center for their assistance in the work outlined in this short review. I would also like to thank Dr. Uğur Özdemir, Dr. Engin Arslan, Dr. Barış Kınacı, and Dr. Ahmet Kürşat Bilgili for his help in this the study.

References

1. A.K. Bilgili, O. Akpınar, M.K. Ozturk, C. Baskose, S. Ozcelik, E. Ozbay, Appl. Phys. A-Matter. **125**(1), 36 (2019). <https://doi.org/10.1007/s00339-018-2338-2>
2. E. Arslan, M.K. Ozturk, S. Ozcelik, E. Ozbay, Philos. Mag. **99**(14), 1715 (2019)
3. T. Ataser, M.K. Ozturk, O. Zeybek, S. Ozcelik, Acta Phys. Pol., A **136**(1), 21 (2019)
4. O. Akpınar, A.K. Bilgili, M.K. Ozturk, S. Ozcelik, E. Ozbay, Appl. Phys. A-Mater. Sci. Process. **125**(2), 112 (2019). <https://doi.org/10.1007/s00339-019-2402-6>
5. A.K. Bilgili, O. Akpınar, M.K. Ozturk, S. Ozcelik, Z. Suludere, E. Ozbay, J. Mater. Sci.-Mater. El. **30**(11), 10391–10398 (2019). <https://doi.org/10.1007/s10854-019-01379-w>
6. M. Demirtas, B. Tamyurek, E. Kurt, I. Cetinbas, M.K. Ozturk, J. Electron. Mater. **48**(11) (2019)
7. U. Ozdemir, S. Korcak, A. Gultekin, M.K. Ozturk, Mater. Res. Exp. **6**(9) (2019)
8. S.V. Novikov, A.J. Kent, C.T. Foxon, Prog. Cryst. Growth Ch. **63**(2), 25 (2017)
9. A.L. Rogach, M.T. Harrison, S.V. Kershaw, A. Kornowski, M.G. Burt, A. Eychmuller, H. Weller, Phys. Status Solidi B **224**(1), 153 (2001)

10. H.M. Tutuncu, E. Karaca, G.P. Srivastava, Phys. Rev. B. **95**(21) (2017)
11. D.A Young, Phase Diagr. Elem. (1991)
12. S.Q. Wang, H.Q. Ye, Phys. Rev. B. **66**(23) (2002)
13. M. Fox, *Optical Properties of Solids*, 2nd edn. (Oxford Master Series in Physics, 2010)
14. H. Akkus, Dissertation, University of Cukurova, 2007
15. A. Gultekin, Dissertation, University of Gazi, 2016
16. D.X. Li, Y. Haga, H. Shida, T. Suzuki, Y.S. Kwon, G. Kido, J. Phys.-Condens. Mat. **9**(48), 10777 (1997)
17. S.M. Hosseini, Phys. B-Condens. Matter. **403**(10–11), 1907 (2008)
18. R. Khenata, A. Bouhemadou, M. Sahnoun, A.H. Reshak, H. Baltache, M. Rabah, Comput. Mater. Sci. **38**(1), 29 (2006)
19. Z. Hongsheng, Y. Tao, W. Deqi, J. Ningxia Univ. (Natural Science Edition) **33** (2012)
20. A. Molchanov, J. Friedrich, G. Wehrhan, G. Muller, J. Cryst. Growth **273**(3–4), 629 (2005)
21. D.A. Neamen, *Semiconductor Physics and Devices Basic Principles* (Mc Graw Hill, 2003), pp. 16
22. G. Singh, B. Ghosh, R.Y. Deshpande, Cryst. Res. Technol. **16**(11), 1239 (1981)
23. M.A. Herman, H. Sitter, Microelectr. J **27**(4–5), 257 (1996)
24. E.C. Kendrick, Dissertation, University of Canterbury, New Zealand, 2008
25. J.M. Olson, M.M. Aljassim, A. Kibbler, K.M. Jones, J. Cryst. Growth **77**(1–3), 515 (1986)
26. E. Arslan, M.K. Ozturk, E. Tiras, T. Tiras, S. Ozelik, E. Ozbay, J. Mater. Sci.-Mater. El. **28**(4), 3200 (2017)
27. S.L. Wong, H.F. Liu, D.Z. Chi, Prog. Cryst. Growth Ch. **62**(3), 9 (2016)
28. S.H. Baxamusa, S.G. Im, K.K. Gleason, Phys. Chem. Chem. Phys. **11**(26), 5227 (2009)
29. F. Kawamura, M. Morishita, K. Omae, M. Yoshimura, Y. Mori, T. Sasaki, Jpn. J. Appl. Phys. **42**(8A), L879 (2003)
30. R.A. Strading, P.C. Klipstein, *Growth and Characterisation of Semiconductor* (IOP Publishing Ltd., 1991)
31. I. Uslu, T. Tunc, M.K. Ozturk, A. Aytimur, Polym-Plast Technol. **51**(3), 257 (2012)
32. S. Rajeshkumar, J. Genetic Eng. Biotechnol. **14**(1), 195 (2016)
33. Y.A. Bioud, A. Boucherif, A. Belarouci, E. Paradis, D. Drouin, R. Ares, Nanoscale Res. Lett. **11**(1), 446 (2016). <https://doi.org/10.1186/s11671-016-1642-z>
34. C. Suryanarayana, M. Grant Norto, *X-Ray Diffraction A Practical Approach* (1998)
35. B.D. Cullity, *Elements of X-Ray Diffraction* (Addison-Wesley Publishing Company, 1956)
36. M.K. Ozturk, H. Altuntas, S. Corekci, Y. Hongbo, S. Ozelik, E. Ozbay, Strain **47**, 19 (2011)
37. D.L. Howard, M.D. de Jonge, D. Lau, D. Hay, M. Varcoe-Cocks, C.G. Ryan, R. Kirkham, G. Moorhead, D. Paterson, D. Thurrowgood, Anal. Chem. **84**(7), 3278 (2012). <https://doi.org/10.1021/ac203462h>
38. M.S. Shackley, *X-Ray Fluorescence Spectrometry (XRF) in Geoarchaeology* (2010)
39. N. Akin, B. Kinaci, Y. Ozen, S. Ozelik, J. Mater. Sci.-Mater. El. **28**(10), 7376 (2017)
40. X.J. Yu, W.H. Wang, L. Li, X.H. Guo, Z.M. Zhou, F.C. Wang, Chinese J. Polym. Sci. **32**(6), 778 (2014)
41. S. Corekci, S. Dugan, M.K. Ozturk, S.S. Cetin, M. Cakmak, S. Ozelik, E. Ozbay, J. Electron. Matter. **45**(7), 3278 (2016)
42. S. Corekci, M.K. Ozturk, M. Cakmak, S. Ozelik, E. Ozbay, Mat. Sci. Semicon Proc. **15**(1), 32 (2012)
43. J. Bai, T. Wang, P.J. Parbrook, K.B. Lee, A.G. Cullis, J. Cryst. Growth **282**(3–4), 290 (2005)
44. N. Faleev, C. Honsberg, O. Jani, I. Ferguson, J. Cryst. Growth **300**(1), 246 (2007)
45. P. Gay, P. Hirsch, A. Kelly, Acta Metall. **1**(3), 315 (1953)
46. T. Ide, M. Shimizu, X.Q. Shen, K. Jeganathan, H. Okumura, T. Nemoto, J. Cryst. Growth **245**(1–2), 15 (2002)
47. D.J. Wolford, G.D. Gilliland, T.F. Kuech, L.M. Smith, J. Martinsen, J.A. Bradley, C.F. Tsang, R. Venkatasubramanian, S.K. Ghandi, H.P. Hjalmarson, J. Vac. Sci. Technol. B **9**(4), 2369 (1991)
48. H.G. Tompkins, E.A. Irene, *Handbook of Ellipsometry*, 1st edn. (Springer, Berlin, 2005)

49. S.S. Cetin, B. Kinaci, T. Asar, I. Kars, M.K. Ozturk, T.S. Mammadov, S. Ozcelik, Surf. Interface Anal. **42**(6–7), 1252 (2010)
50. B. Kinaci, Y. Ozen, T. Asar, S.S. Cetin, T. Memmedli, M. Kasap, S. Ozcelik, J. Mater. Sci.-Mater. El. **24**(9), 3269 (2013)
51. C. Sancar, Dissertation, University of Gazi, 2004
52. S. Perkowitz, *Optical Characterization of Semiconductors: Infrared, Raman, And Photoluminescence Spectroscopy* (Academic Press, London, San Diego, 1993)
53. S. Ozkaya, Dissertation, University of Gazi, 2005
54. T. Ataser, Dissertation, Balikesir University, 2017
55. J.R. Ferraro, K. Nakamoto, *Introductory Raman Spectroscopy*, 1st edn. (Academic Press, San Diego, 1994)
56. D. Long, *Raman Spectroscopy* (Mc Graw Hill, New York, 1971)
57. J. Bardeen, W.H. Brattain, Phys. Rev. J. Archive **74**(2), 230 (1948)
58. J.F. Suyver, Dissertation, University of Utrecht, 2003
59. M. Gallignani, M.D. Brunetto, Talanta **64**(5), 1127 (2004)
60. A.K. Bilgili, O. Akpınar, G. Kurtulus, M.K. Ozturk, S. Ozcelik, E. Ozbay, XRD vs raman for InGaN/GaN structures. J. Polytechnic. (2019). <https://doi.org/10.2339/politeknik.537733>
61. K. Heilig, Hyperfine Interact. **24**(1–4), 349–375 (1985)
62. C.P. Constable, D.B. Lewis, J. Yarwood, W.D. Münz, Surf. Coat. Technol. **184**(2–3), 291–297 (2004)
63. G.B. Kilic, A.G. Karahan, J. Food **35**(6), 445 (2010)
64. K. Nakamoto, *Infrared and Raman Spectra of Inorganic and Coordination Compounds*, 5th edn. (A Wiley-Interscience Publication, New York, 1997)
65. N. Puviarasan, V. Arjunan, S. Mohan, Turk. J. Chem. **26**(3), 323 (2002)
66. H.U. Gremlich, *Infrared and Raman Spectroscopy of Biological Materials* (New York, 2001)
67. M.G. Rockley, D.M. Davis, H.H. Richardson, Science **210**(4472), 918 (1980)
68. B. Stuart, *Infrared Spectroscopy: Fundamentals and Applications* (Wiley, Hoboken, 2004)
69. L.I. Maklakov, G.G. Suchkova, Spectrochim Acta A. **71**(1), 238 (2008)
70. A.R.W. McKellar, D.R.T. Appadoo, J. Mol. Spectrosc. **250**(2), 106 (2008)
71. B.J. Reddy, R.L. Frost, S.J. Palmer, Spectrochim Acta A. **71**(2), 430 (2008)
72. T.W. Graham Solomons, *Craig Barton Fryhle Organic Chemistry*, 7th edn. (Wiley, London, 2001)
73. A. Yildiz, Ö. Genç, *Instrumental Analysis* (Hacettepe University Publications, 1993)
74. J.Y. Lin, B.X. Wang, Adv. Mater. Sci. Eng. **6**, 594516 (2014). <http://dx.doi.org/10.1155/2014/594516>
75. H.H. Perkampus, *UV-VIS Spectroscopy and Its Applications* (Springer Laboratory, Berlin, 1992)
76. S. Kumar, V. Gupte, K. Sreenivas, J. Phys.-Condens. Mat. **18**(13), 3343 (2006)